

## Topical Review

# Defect-induced magnetism in SiC

Shengqiang Zhou<sup>1</sup>  and Xiaolong Chen<sup>2,3,4</sup>

<sup>1</sup> Helmholtz-Zentrum Dresden-Rossendorf, Institute of Ion Beam Physics and Materials Research, Bautzner Landstrasse 400, D-01328 Dresden, Germany

<sup>2</sup> Research & Development Center for Functional Crystals, Laboratory of Advanced Materials & Electron Microscopy, Beijing National Laboratory for Condensed Matter Physics, Institute of Physics, Chinese Academy of Sciences, Beijing 100190, People's Republic of China

<sup>3</sup> University of Chinese Academy of Sciences, Beijing 100049, People's Republic of China

<sup>4</sup> Collaborative Innovation Center of Quantum Matter, Beijing 100084, People's Republic of China

E-mail: [s.zhou@hzdr.de](mailto:s.zhou@hzdr.de) and [chenx29@iphy.ac.cn](mailto:chenx29@iphy.ac.cn)

Received 9 January 2019, revised 3 May 2019

Accepted for publication 24 May 2019

Published 18 July 2019



### Abstract

Defect-induced magnetism describes a magnetic phenomenon in materials containing neither unpaired 3d nor 4f electrons. Therefore, it presents a challenge to the conventional understanding of magnetism and has remained under debate for over a decade. Different from graphite and oxides which are common research venues in defect-induced magnetism, SiC is commercially available at large scale and with high quality at the microelectronic grade. Therefore, SiC presents a suitable model system for studying defect-induced ferromagnetism and exploring possible applications. Understanding and controlling defect-induced magnetism in a semiconductor like SiC opens up the possibility for producing spintronic devices based on classical semiconductor technologies. Here, we review recent studies on defect-induced magnetism in SiC. We start with a brief description about defects in SiC. Then we summarize the experimental results on defect-induced magnetism in SiC, the microscopic origin of the magnetism and the magnetic coupling mechanism. We also propose several potential applications, particularly using magnetometry as a complementary method for quantitative characterization of defects in SiC. At the end, we list the challenges from our point of view, such as controlling defects in SiC regarding their charge states, distribution and local environment, and understanding defect-induced magnetism by local and elemental selective probe techniques.

Keywords: SiC, defects, magnetism

(Some figures may appear in colour only in the online journal)

### 1. Introduction

Over the last decade, the study of dilute magnetic semiconductors has undergone a transition from doping 3d elements to creating defects in the host semiconductor. This is, in particular, true for SiC. On one hand, since SiC has a very rigid lattice, the solid solubility of 3d elements is very limited. The observed ferromagnetism at varying temperatures is often debated. The focus of the debate lies in whether the magnetism really comes from the intrinsic doped SiC or from other sources, such as resultant secondary phases or 3d metal

precipitates. These secondary phases and precipitates, though in a tiny amount, can often be responsible for the observed magnetism. For instance, it has been demonstrated that the main source of the magnetism in Fe-implanted SiC is due to the secondary phase Fe<sub>3</sub>Si using atomic probe tomography and <sup>57</sup>Fe Mössbauer spectroscopy [1, 2].

On the other hand, it is well known that localized magnetic moments and the coupling between them are two indispensable factors to induce long-range spin ordering in solids, such as ferromagnetism, antiferromagnetism, ferrimagnetism, etc. Previously, only atoms that contain partially filled 3d or 4f

subshells were thought to produce local moments according to Hund's rule. Spontaneous spin coupling tends to occur and leads to various long-range orderings depending on the nearest- and next-nearest spin–spin exchange integrals. In general, the coupling strength is sensitive to the separation of the spins. Coupling over a large separation is possible if the wave functions have sufficient spatial extent. This is the case for dilute magnetic semiconductors, where the concentrations of  $3d$  metals are in a range from less than one to a few atomic percent and the free carriers mediate the magnetic coupling [3]. Recently, however, evidence has been accumulating that the intrinsic magnetism can come from certain kinds of defects in a variety of solids. For instance, room temperature ferromagnetism was observed in highly oriented pyrolytic graphite [4–6], in  $\text{HfO}_2$  [7], in Al-doped SiC [8], in Li-doped  $\text{ZnO}$  [9], and in various nano-sized compounds [10, 11] that are otherwise nonmagnetic in their bulk states. See [12–14] for recent reviews.

Different from graphite and oxides which are common research venues in defect-induced magnetism, SiC is commercially available at large scale and with high quality at the microelectronic grade. Therefore, SiC presents a suitable model system for studying defect-induced ferromagnetism and for exploring possible applications. Here, we review recent studies on defect-induced magnetism in SiC. We also propose potential applications and list the challenges in controlling defect-induced magnetism in SiC from our point of view.

## 2. Introducing defects in SiC

SiC is a wide-bandgap semiconductor, belonging to the class of third-generation semiconductors. Due to its outstanding properties such as high thermal conductivity, high breakdown voltage and high saturated electron drift velocity, SiC is steadily replacing conventional semiconductor materials, e.g. silicon (Si) and gallium arsenide (GaAs) for certain extreme applications [15]. Therefore, to understand and control the defects is interesting in general. When talking about defects in SiC, one has to note its large number of polytypes [16]. Up to now, more than 200 types of phases of SiC have been found. The technically interesting polytypes are 4H-, 6H- and 3C-SiC. Both 4H- and 6H-SiC are hexagonal and have bandgaps of 3.26 and 3.02 eV, respectively [17]. 3C-SiC is cubic and also called  $\beta$ -SiC with a bandgap of 2.4 eV [17].

High-purity SiC (doping less than  $10^{16} \text{ cm}^{-3}$ ) has been grown by high-temperature chemical vapor deposition, physical vapor transport and chemical vapor deposition (CVD). Extended defects in SiC include (1) open-core dislocations (also known as micropipes), (2) low-angle boundaries and (3) conventional dislocations [18]. However, those extended defects are not within the scope of this review, although they may play an important role in the magnetic coupling. In the current review, we focus on point defects, like vacancies, interstitials, anti-sites and their complexes [19]. Those point defects can have spin and therefore act as local moments. As

**Table 1.** Spin values for the stable charge states of the  $\text{N}_C\text{V}_{Si}$ ,  $\text{V}_{Si}$  and  $\text{V}_C$  defects in 4H-SiC. From [20].

Charge state	$\text{N}_C\text{V}_{Si}$	$\text{V}_{Si}$	$\text{V}_C$
+2	Unstable	Unstable	0
+1	Unstable	Unstable	1/2
0	1/2	1	0
-1	1	3/2	3/2
-2	1/2	1	0

an example, Weber *et al* [20] calculated the spin values for different defects in 4H-SiC, as listed in table 1.

### 2.1. By changing growth condition

Bechstedt *et al* studied the prototypical native defects, in particular monovacancies, in 3C- and 4H-SiC using *ab initio* density functional theory and local spin-density approximation [21]. Carbon vacancies with 2+ charge have the lowest formation energies (hence, the highest defect concentrations) under p-type doping and both Si-rich and C-rich preparation conditions. Carbon vacancies are double donors and dramatically reduce the doping efficiency of acceptors.

Therefore, electrically active defects in SiC depend strongly on the growth conditions. Experimentally, the main variables are the growth temperature, the growth pressure and the C/Si pressure ratio. Kimoto *et al* grew 4H-SiC by a horizontal hot-wall CVD system under different reactor pressures and different C/Si ratios [22]. The electron concentration (for unintentionally doped samples) increases with increasing the reactor pressure. The total trap concentration is also reduced by increasing the input C/Si ratio. Another work from the same group again confirms that the C-rich condition is favorable to reduce intrinsic defects [23].

Zhang *et al* investigated electrically active defects in epilayers grown with fast epitaxy by a vertical, hot-wall CVD reactor [24]. They found intrinsic defects and impurities such as B and Ti in most of the epilayers. The intrinsic defect concentration increases with the growth temperature. The incorporation of shallow B impurities is enhanced at lower temperatures and can be increased by increasing the C/Si ratio. The Ti concentration does not show a clear temperature dependence, but increases with increasing the C/Si ratio. The concentrations of EH6/7 (electron traps) and HS1 (hole traps) are reduced at higher C/Si ratio, and the  $Z_{1/2}$  (electron traps) concentration is not sensitive to the C/Si ratio [24].

### 2.2. By ion irradiation

With the advances in accelerator technologies, a variety of ions (all stable elements and some radioactive elements) in a wide energy range from eV to hundreds of GeV can be produced and injected into targets. Using the chemical effect of injected ions, the ‘ion implantation’ technique is a common method of doping semiconductors. This technique has been integrated into the standard microelectronics production line for integrated circuits in silicon technology. Ion irradiation

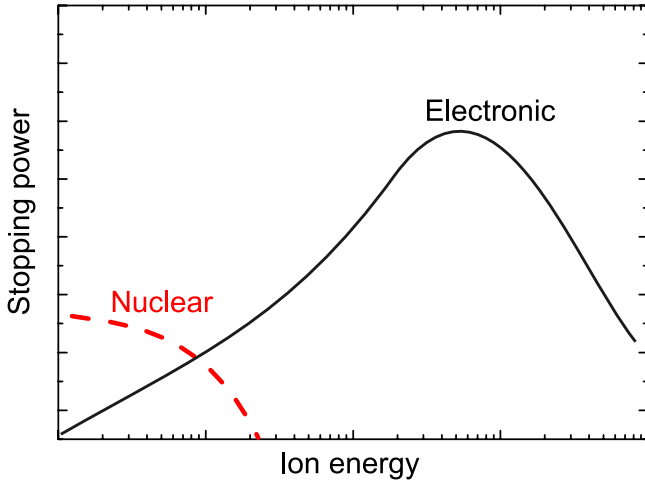


**Figure 1.** Schematic of the cross-section for electronic and nuclear stopping processes as a function of ion energy [25].

refers to using other effects rather than the doping effect in materials. Compared with varying growth and/or annealing parameters to control defects in SiC, the use of an ion beam has a number of advantages:

- High speed and reproducibility;
- Exact control of the implantation fluence by integration of the beam current;
- Exact control of the implantation energy to generate defects at different depths;
- Simple masking methods to make lateral patterns for devices.

The ions implanted into a semiconductor undergo collisions with the target atoms, and lose their energies due to the ion stopping process. The total energy loss per unit distance is determined by the electronic stopping and the nuclear stopping. In the former process, the ion energy is lost by excitation and ionization of atoms (inelastic). The lost energy eventually dissipates as heat, and does not create atomic displacements in the materials. The electronic stopping cross-section is proportional to the velocity of the ions. Its contribution dominates in the high-energy regime. Nuclear stopping occurs as a result of elastic collisions of ions with nuclei in the target, and leads to atomic displacements. These displaced atoms may have enough energy to displace others, resulting in a cascade of recoiled atoms. Nuclear energy loss dominates at intermediate energies (hundreds of keV), and leads to the creation of deep-level compensating defects. At high energies, the contribution from nuclear stopping tends to be small because fast ions have only a short time to interact with a target nucleus, and cannot transfer energy efficiently. Figure 1 shows a schematic of the relative energy loss due to electronic and nuclear stopping processes as a function of ion energy.

One of the most important parameters that determines the extent of lattice damage is the threshold displacement energy,  $E_d$ . This is defined as the minimum kinetic energy to be transferred to an atom to displace it from its lattice site, resulting in a stable Frenkel pair. Devanathan and Weber used molecular dynamics simulations to calculate  $E_d$  in 3C- and 6H-SiC

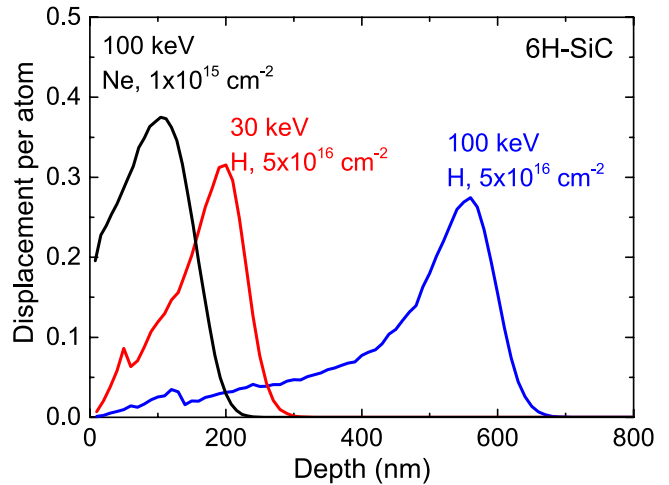


**Figure 2.** SRIM simulation of dpa in 6H-SiC for 30 keV and 100 keV H ion implantation at the fluence of  $5 \times 10^{16} \text{ cm}^{-2}$ , and for 100 keV Ne ion implantation at the fluence of  $1 \times 10^{15} \text{ cm}^{-2}$ . The heavier ions at lower energy produce many more defects than light ions.

[26]. The two polytypes show many similarities in the nature of the  $E_d$  surface. The minimum displacement energies are 21 eV for C and 35 eV for Si in both 3C-SiC and 6H-SiC, and the values are in good agreement with the interpretation of experimental observations. One of the drawbacks of using ion beams to create defects is the lack of selectivity for producing specific defects. Particularly, in compound semiconductors ion irradiation always produces many kinds of defects, such as vacancies and interstitials of each constituent element as well as antisites.

The stopping and range of ions in matter (SRIM) is the most comprehensive program available to calculate the interactions between ions and matter. This is a Monte Carlo program developed by Ziegler and Biersack [25], which will calculate both the total three-dimensional distribution of the ions and also all kinetic phenomena associated with the ion's energy loss: target damage, sputtering, ionization and phonon production. An example is given in figure 2 for hydrogen and neon ion-implanted 6H-SiC. The distributions of the radiation damage have been estimated from Monte Carlo calculations using SRIM2003 with a density of  $3.21 \text{ g cm}^{-3}$  and displacement energy of 21 eV for C and 35 eV for Si. The displacement per atom ( $dpa$ ) is calculated as:  $dpa = \text{implantation fluence} \times \text{displacements per ion and unit depth} / \text{atomic density}$ , where the displacements are calculated by the SRIM code. By varying the ion energy, one can place the defect at different depths. Heavier ions (here Ne) produce many more defects than light ions. Note that the SRIM code does not take into account the recombination of the primary interstitials and vacancies and thus the actual damage levels in the sample can be lower than the simulated values.

### 2.3. By electron irradiation

Energetic electrons interact with the nuclei and the electron system in the target. Because of momentum conservation, only a small fraction of the impinging electron energy can be

transferred to a nucleus. Comparing with ions, a rather high electron energy ('threshold energy') is needed to displace an atom. The energy is transferred via electron–nucleus scattering. For example, an electron energy of 100 keV is needed to transfer around 20 eV to a carbon atom. This is close to the threshold for moving the carbon atom in the graphitic structure [27]. Note that displacement energies in SiC are 21 eV and 35 eV for C and Si, respectively. On the other hand, electron–electron scattering already occurs at low electron energies and may cause ionization or bond breaking. Normally, this kind of energy transfer does not result in atom displacements but may introduce defects in the target due to beam-stimulated local chemical reactions. The cross-sections of both nuclear and electron scattering decrease with the increasing electron energy.

It is interesting to note that for SiC, the Si/C mass ratio is around 2.33, resulting in clearly separated irradiation energy thresholds for the displacements of different lattice atoms. It has been suggested that the threshold energies of an electron to displace C and Si in SiC are 100 and 250 keV, respectively [28]. Therefore, with low-energy electron irradiation in the 100–250 keV range, one can create only those intrinsic defects related to the initial displacements of carbon atoms in the SiC [29].

#### 2.4. By neutron irradiation

Neutrons are uncharged particles. Therefore, neutrons have no interaction with atomic electrons, but only interact with nuclei in the material. The nuclear force, leading to the interaction between neutrons and nucleus, is very short ranged. Given the fact that the size of the nucleus in relation to the atom is very small, neutrons have low probability of interaction and can penetrate a very large distance before being slowed down. The process of creating crystal lattice damage during neutron irradiation is due to the scattering of the energetic neutrons by the nuclei of the target atoms. The neutrons are generally produced by nuclear fission and their energies extend over a wide range of energy from meV to around 10 MeV, with a mean energy of 2 MeV. The displacement energy thresholds of C and Si in SiC are in the order of 20 and 30 eV, respectively. It is reasonable to assume that the transferred energy from the neutron to the nucleus, which will irreversibly displace the lattice atoms from their site, will be a few times the displacement threshold. Neutrons with energies larger than about 100 eV (including epithermal neutrons with energy 50 eV–500 keV and fast neutrons with energy 50 keV–10 MeV [30]) can produce displacements and the displaced atoms with greater energies produce further displacements in collisions with other target atoms in a cascade. The elastic scattering dominates when the energy is below 5.5 MeV in carbon and the nuclear reaction (inelastic scattering) only becomes significant when the energy is above 9 MeV [31].

As an example, at the DBVK chamber at the BER II reactor at Helmholtz-Zentrum Berlin, the fluxes are  $1.08 \times 10^{14} \text{ cm}^{-2} \text{ s}^{-1}$  for thermal neutrons below 50 eV,  $7.04 \times 10^{12} \text{ cm}^{-2} \text{ s}^{-1}$  for epithermal neutrons, and  $5.80 \times 10^{13} \text{ cm}^{-2} \text{ s}^{-1}$  for fast

neutrons. Comparing with epithermal or fast neutrons, thermal neutrons only produce negligible displacement. Therefore, only epithermal and fast neutrons are accounted for in the fluence calculation.

#### 2.5. Comments on different irradiation methods

Ions are available at implanters. High-energy electrons can be produced by accelerators and low-energy electrons are also available at scanning electron microscopy and transmission electron microscopy. Those facilities are generally accessible at many universities/research institutes. However, neutron sources are limited at nuclear reactors with limited availability and access. One also has to note that neutrons also induce activation of heavy elements. After neutron irradiation, the samples have to be checked until they decay to a safe level before the structural, electrical and magnetic measurements can be performed.

On the other hand, the microscopic structure of most of the defects created by irradiation is poorly understood. This is not surprising, since the number of possible defect configurations created by high-energy particles is huge and difficult to treat. In many cases, it is not even known which atom—carbon or silicon or both—is involved in the formation of the defect center. Electron irradiation gives the possibility to selectively induce defects in SiC since the displacement threshold energy to move Si or C is very different.

We also should know the collision cross-section of different irradiation sources with SiC; in other words, the possibility of inducing defects. As a rule of thumb, ions have the largest possibility due to their large mass in comparison with electrons. Neutrons have the smallest cross-section since only strong interaction is involved. As an example, the cross-section of MeV neutrons is smaller than MeV Ar ions by around four orders of magnitude [32].

#### 2.6. Identifying defects

To measure defects in SiC, different methods have been well developed for samples with different defect concentrations. For irradiation-induced defects, a useful parameter to quantify the amount of defects is the displacement of lattice atom (*dpa*). The *dpa* is calculated as:  $dpa = \text{implantation fluence} \times \text{displacements per ion and unit depth} / \text{atomic density}$ , where the displacements can be calculated by the SRIM code [25].

In figure 3, we schematically compare different measurement techniques regarding the applicable defect concentration. Rutherford backscattering/channeling spectroscopy (RBS/C) is generally sensitive to point defects at relatively high concentration, but struggles to identify the nature of the defects, i.e. single vacancy or double vacancy. Transmission electron microscopy is powerful in detecting extended defects, but struggles to find point defects at low concentrations. Electron paramagnetic resonance [33, 34] and optically detected magnetic resonance [35] are sensitive in identifying point defects in SiC. Hyperfine interaction due to  $^{29}\text{Si}$  and  $^{13}\text{C}$  is decisive

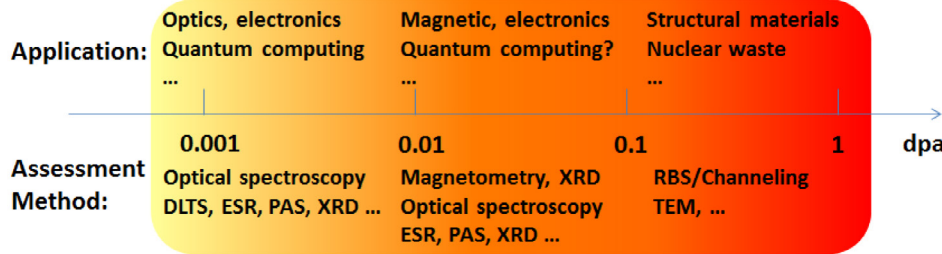


**Figure 3.** Schematic representation of the investigation of defects in irradiated SiC concerning applications and assessment methods. DLTS: deep-level transient spectroscopy; ESR: electron spin resonance; PAS: positron annihilation spectroscopy; XRD: x-ray diffraction; RBS/channeling: Rutherford backscattering/channeling; TEM: transmission electron microscopy.

information, which can be used to extract not only the chemical identity but also the local geometry and the electronic state of defects.

Photoluminescence, particularly the zero-phonon line (ZPL), is also the fingerprint of different point defects. For instance, in 4H-SiC the ZPL was calculated for different divacancies: the  $kk$  and  $hh$  forms of the axial divacancy ( $k$  stands for quasicubic position and  $h$  for quasihexagonal), and the  $kh$  and  $hk$  forms of the basal divacancy. The energies of ZPL can be used to distinguish the four forms of divacancy [36]. The calculation is in good agreement with experimental results [37].

Deep-level transient spectroscopy (DLTS) is a suitable technique to investigate electrically active point defects in SiC [38–40]. The defects reflect themselves as DLTS peaks in the spectrum as a function of temperature. Carbon vacancies have been clarified to be the major electrically active defects in 4H-SiC and they are serious obstacles for high-voltage bipolar devices [41].

For the above-mentioned methods, we recommend different review or research articles cited in this manuscript. We will introduce a little more information on positron annihilation spectroscopy (PAS) [42]. PAS has been used as a non-destructive probe in semiconductors because of its high sensitivity to neutral or negatively charged vacancies and vacancy clusters. Vacancies in the semiconductor can trap implanted positrons into localized states which have a longer positron lifetime compared to delocalized positrons, since the electron density at the vacancy site is lower. Different vacancies can be identified by their characteristic positron lifetimes, which are fingerprints of the corresponding defects.

Figure 4 shows typical positron lifetime spectra in electron-irradiated SiC [43]. In this measurement, the lifetimes of a huge amount of positrons are recorded by detecting the birth of the positron and the subsequent radiation emitted by annihilation. In other words, the lifetime is the delay between the position emission and annihilation. Positrons annihilate at different lattice sites. Each of them has a characteristic lifetime. Since annihilation is a statistical process, many annihilation events have to be recorded and are placed in a histogram in order to determine the positron lifetime in the measured specimen. The intensity (or counts) represents the annihilation events at a particular time. It is often given in a relative manner. From figure 4, one can see the lifetime increases with the irradiation fluence. Generally, a multi-component fit was used

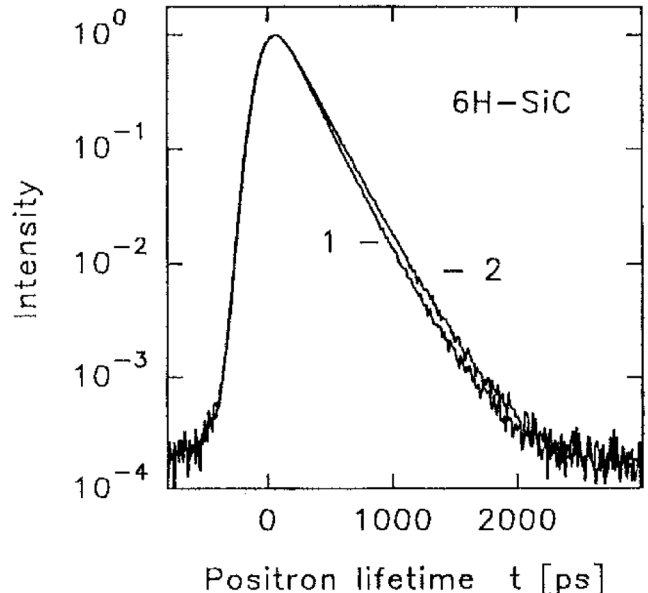


**Figure 4.** Positron lifetime spectra in low-temperature electron-irradiated 6H-SiC with the following electron energies and irradiation fluences ( $\phi$ ): 1— $E = 2.5$  MeV and  $\phi = 1.3 \times 10^{18}$  e cm $^{-2}$ ; 2— $E = 2.5$  MeV and  $\phi = 1.2 \times 10^{19}$  e cm $^{-2}$ . [43] © Springer-Verlag 1995. With permission of Springer.

to separate different contributions in the spectra. In these two particular spectra shown in figure 4, two life components were obtained. One is the short component  $\tau_1 \sim 159$  ps which is very close to the free lifetime due to single vacancies. The second component  $\tau_2 \sim 210$  ps is due to divacancies. A similar lifetime  $\tau_2 \sim 225$  ps was also measured by Ling *et al* and was attributed to divacancies in doped 6H-SiC [44, 45]. Brauer *et al* investigated the positron lifetime in vacancy clusters in 3C-SiC and 6H-SiC [46]. The lifetime increases with the size of vacancy clusters. In ion-implanted SiC, the positron lifetime also increases with increasing ion fluence, indicating the divacancy clustering and crystalline amorphization [47].

In addition to identifying the defect types, the multi-component fitting for the lifetime spectra also gives the intensity of each component. The intensity carries information on the defect concentration. Figure 5 shows  $\tau_2$  and its intensity as a function of the positron energy. It also provides the depth distribution of the defects. By knowing the positron trapping rate of a particular defect, one can calculate the defect density through the procedure described in [47] and its depth profile.

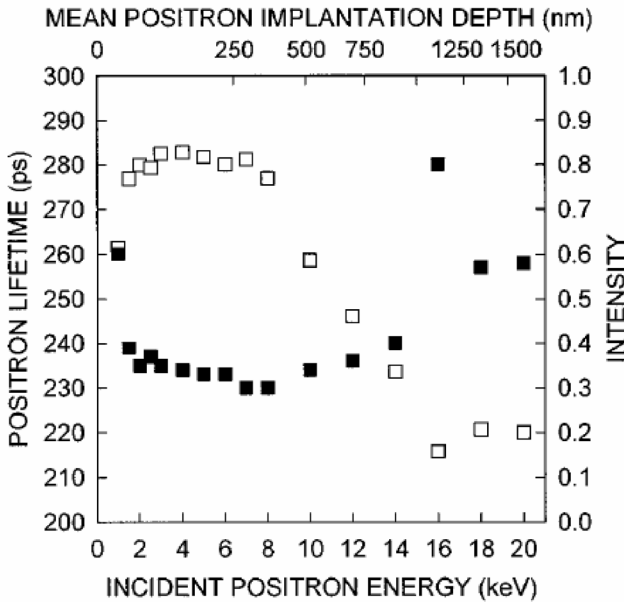


**Figure 5.** Second positron lifetime  $\tau_2$  (solid squares, left y axis) and its relative intensity  $I_2$  (open squares, right y axis) as a function of incident positron energy  $E$  for 200 keV Ge implanted 6H-SiC with the fluence of  $1 \times 10^{17} \text{ cm}^{-2}$ . The depth is estimated and shown as the top x axis. Reprinted figure with permission from [47]. Copyright 1996 by the American Physical Society.

It was estimated that the divacancy concentration in the damaged layer (the top 300 nm) is 44 ppm in this particular sample shown in figure 5. Indeed, the lifetime measurement was also done for neutron-irradiated, ferromagnetic SiC [48], as shown later in figure 10.

Besides the lifetime, positron annihilation Doppler broadening spectroscopy is also able to identify the defect type. When positrons annihilate with electrons, two 511 keV photons are emitted. The Doppler broadening of the 511 keV gamma emission peak is mainly caused by the momentum of the electron due to the very low momentum of the thermalized positron, and is characterized by the line-shape parameter  $S$  [49]. The value of  $S$  is defined as the ratio of counts in the central region of the annihilation gamma peak to the total number of counts in the peak. The energy regions are selected to give  $S = 0.5$  for the virgin bulk material and are then fixed for the irradiated samples. The  $S$ -parameter characterizes the positron annihilation with low momentum electrons and it increases with the increasing size of the particular open volume defects (e.g. vacancy clusters). In [47], the authors have shown that  $V_{Si}-V_C$  divacancies in 6H-SiC can be identified by an  $S$ -parameter of 0.5375. In [49], the authors established a relationship between the number of clustered divacancies and the  $S$ -parameter.

Figure 6 shows the measured  $S$ -parameter versus the incident positron energy for 500 keV Xe-irradiated 6H-SiC. The maximum of the  $S$  parameter around the positron energy of 3–4 keV corresponds to positron annihilation in the defects created by ion implantation within a depth of about 200 nm. For higher positron energies the positron annihilation is shifted more and more to the undamaged bulk material, the  $S$ -parameter decreases and finally reaches the bulk value at 20 keV (dash-dot line in figure 6). The  $S$ -parameter of the  $V_{Si}-V_C$

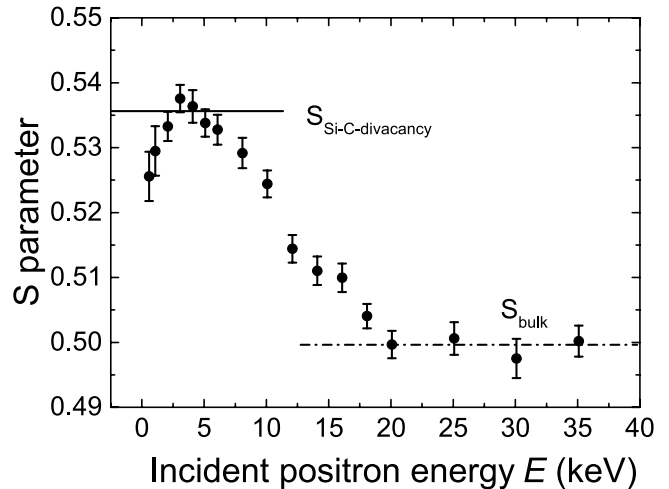


**Figure 6.**  $S$ -parameter versus incident positron energy of the Xe-implanted 6H-SiC sample at the energy of 500 keV and the fluence of  $5 \times 10^{12} \text{ cm}^{-2}$ . Reproduced from [50]. CC BY 4.0.

divacancy is plotted as a solid line in figure 6. The  $S$ -parameter of the defects in the Xe ion-irradiated sample agrees well with that for the  $V_{Si}-V_C$  divacancy.

In this section, we have briefly discussed different methods to characterize defects in SiC. However, one has to note that SiC is a binary compound semiconductor. The displaced atoms and implanted ions have many different possibilities to occupy substitutional, interstitial and anti-sites. This eventually results in many features in the measurement spectrum and makes it difficult to assign the features to the structural defects. Further, many inequivalent lattice sites can also lead to a broad, featureless spectrum. Therefore, to identify the structural defects first-principle calculations are often needed. Moreover, different experimental techniques should be used and the results should be compared.

### 3. Defect-induced magnetism in SiC

#### 3.1. Ferromagnetism

The first report on magnetism in SiC which is not doped with transition metal concerns the glassy ferromagnetism in Al-doped 4H-SiC, as shown in figure 7. In this work by Song *et al* [8], magnetic hysteresis was observed for single-phase Al-doped 4H-SiC at room temperature, but not observed for undoped samples down to 4 K. The sample was prepared by single crystal growth with Al concentration of  $\sim 0.75$  atom%. Zero-field-cooled (ZFC) and field-cooled (FC) temperature dependence of dc magnetization at different fields was measured. At low field, a pronounced ZFC–FC irreversibility is revealed and the irreversibility becomes weaker with increasing the applied field. These features are the fingerprints for spin glass systems.

The authors proposed that the formation of local magnetic moments in Al-doped 4H-SiC is related to the conversion from carbon  $sp^3$  to  $sp^2$ . Upon Al doping in SiC, some C–Si bonds ( $sp^3$  configuration with a bond energy of  $301 \text{ kJ} \cdot \text{mol}^{-1}$ ) can be converted to C–Al bonds in  $sp^2$  plane configuration. The trivalent Al ions substitute Si sites, leading to a mixture of

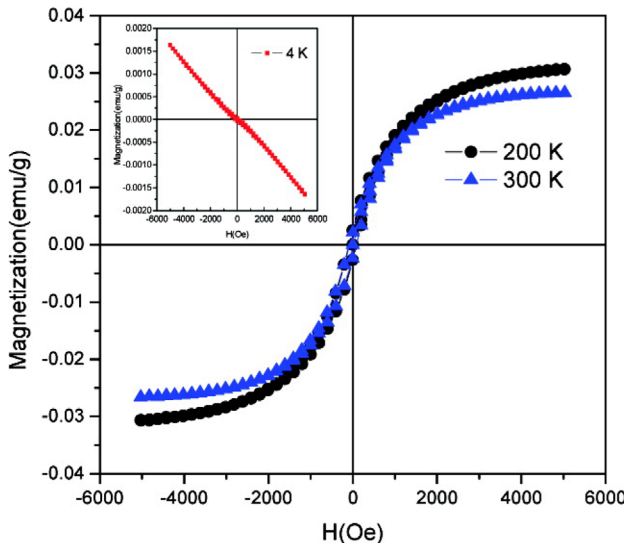


**Figure 7.** Hysteresis loops for Al-doped 4H-SiC, observed at 200 K (circles) and 300 K (triangles). The inset shows the hysteresis loops at  $T = 4$  K (squares) for the undoped 4H-SiC obtained at the same experimental conditions. Reprinted with permission from [8]. Copyright (2009) American Chemical Society.

$sp^3/sp^2$  hybridization. The unpaired electron is prompted to a higher orbital, enabling it to participate in the magnetic ordering. To induce the ferromagnetic coupling, a strong enough correlation between these local spins must exist. The authors suggested that the structural defects induced by Al doping can serve as this mediation. Later, a study by means of first-principles calculations suggested that the complex of substitution Al for Si together with a Si vacancy can induce spin polarization and local magnetic moments in Al-doped 4H-SiC [51]. The interaction between the local moments results in the ferromagnetic order.

Liu *et al* reported defect-induced magnetism in neutron-irradiated 6H-SiC single crystals [48]. In this work, a correlation between structure and magnetism was given in detail. The starting samples are commercially available 2 inch semi-insulating p-type 6H-SiC (0001) wafer. The neutron fluence was varied from  $1.91 \times 10^{17} \text{ n cm}^{-2}$  to  $2.29 \times 10^{18} \text{ n cm}^{-2}$ . Figure 8 shows the magnetization with varied applied field at 5 K. In the pristine sample, only diamagnetic features have been observed. After a low-fluence irradiation at  $1.91 \times 10^{17} \text{ n cm}^{-2}$ , a weak hysteresis loop can be seen in the low-field range. With increasing irradiation fluence, the diamagnetism becomes weaker and the hysteresis loops arise. At a fluence of  $2.29 \times 10^{18} \text{ n cm}^{-2}$ , a distinct hysteresis loop can be clearly observed as shown in figure 8(b). The saturation magnetization reaches  $1 \times 10^{-4} \text{ emu g}^{-1}$ . Even at 300 K, the hysteresis loop can still be observed as shown in figure 8(c). It is suggested that the ferromagnetism is not homogeneously distributed but probably exists in domains. Therefore, the magnetization values obtained by dividing the magnetic moment by the total mass do not correspond to the expected intrinsic values.

The defective structure in this neutron-irradiated 6H-SiC was investigated by Raman scattering, as shown in figure 9(a). The decrease in Raman intensity for each mode with

increasing irradiation fluence is a direct reflection of the lattice damage. Figure 9(b) shows the relative intensity variation of the folded longitudinal optical mode given by  $(1/I_0)$  versus fluence, where  $I_0$  and  $I$  are the intensities of the peak measured in the pristine and irradiated samples, respectively. Such a change in the relative intensity suggests the existence of defects in the irradiated samples.

To investigate the nature of defects created by neutron irradiation, positron annihilation lifetime spectroscopy was performed. The lifetime spectrum was obtained and decomposed into lifetimes correlated with different annihilation sites. The fitted positron lifetimes  $\tau_1$ ,  $\tau_2$ , and the fraction of the defects with longer lifetime ( $\tau_2$ )  $I_2$  as functions of the irradiation fluence are shown in figure 10. It is found that the lifetimes  $\tau_1$  around  $130 \pm 14 \text{ ps}$  and  $\tau_2$  around  $239 \pm 20 \text{ ps}$  are independent of irradiation fluence, and  $I_2$  is proportional to the irradiation fluence within the fluence range applied in this study. The lifetime value of  $130 \pm 14 \text{ ps}$  can be assigned to the bulk lifetime of 6H-SiC. The positron trapping center at  $239 \pm 20 \text{ ps}$  is close to  $253 \pm 4 \text{ ps}$  and  $225 \pm 11 \text{ ps}$ . It is suggested to be the  $V_{Si}-V_C$  divacancy in 6H-SiC crystals. The dependence of  $I_2$  on the irradiation fluence suggests that the concentration of  $V_{Si}-V_C$  increases with the fluence.

Therefore, considering the full picture shown in [48], it is reasonable to correlate the magnetism with the  $V_{Si}-V_C$  divacancies. In a follow-up work by Wang *et al* [52], a much broader range of neutron fluence was applied. It was found that the paramagnetic component dominates and the ferromagnetic component is relatively weak.

Almost at the same time, 6H-SiC single crystals have been shown to be ferromagnetic after bombardment using ions [53]. In this work,  $Ne^+$  ions at an energy of 140 keV have been implanted at different fluence from  $5 \times 10^{13}$  to  $1 \times 10^{15} \text{ cm}^{-2}$ , denoted as 5E13–1E15, respectively. As shown in figure 11, the virgin SiC shows only diamagnetism. After Ne implantation (1E14), a ferromagnetic contribution appears. The as-measured magnetic moment is at the order of  $10^{-4} \text{ emu}$  for a sample of  $5 \times 5 \text{ mm}^2$ . Note that the volume (sample thickness) affected by ion irradiation is much smaller compared with neutron irradiation. Figure 12 shows the ferromagnetic hysteresis loop after subtracting the diamagnetic background for samples with different fluences. An initial increase in structural disorder leads to pronounced ferromagnetic properties at room temperature. Further introduction of disorder reduces the saturation magnetization and at the same time the crystallinity of SiC is decreased. Close to the threshold of full amorphization [54], the saturation magnetization nearly drops to zero.

The picture from lattice damage to amorphization of SiC upon Ne ion implantation has been corroborated by RBS/C. The ion-implantation-induced atomic disorder of the Si sublattice in 6H-SiC is quantitatively determined. Damage accumulation on the carbon sublattice is expected to exhibit similar behavior according to SRIM full-damage cascade simulations. The RBS/C spectra along SiC[0001] are shown in figure 13 for the unirradiated (virgin) and for the same set of samples shown in figure 12. A random spectrum is also shown for comparison. The random spectrum is assumed to be equivalent to a completely amorphized SiC, while the virgin spectrum

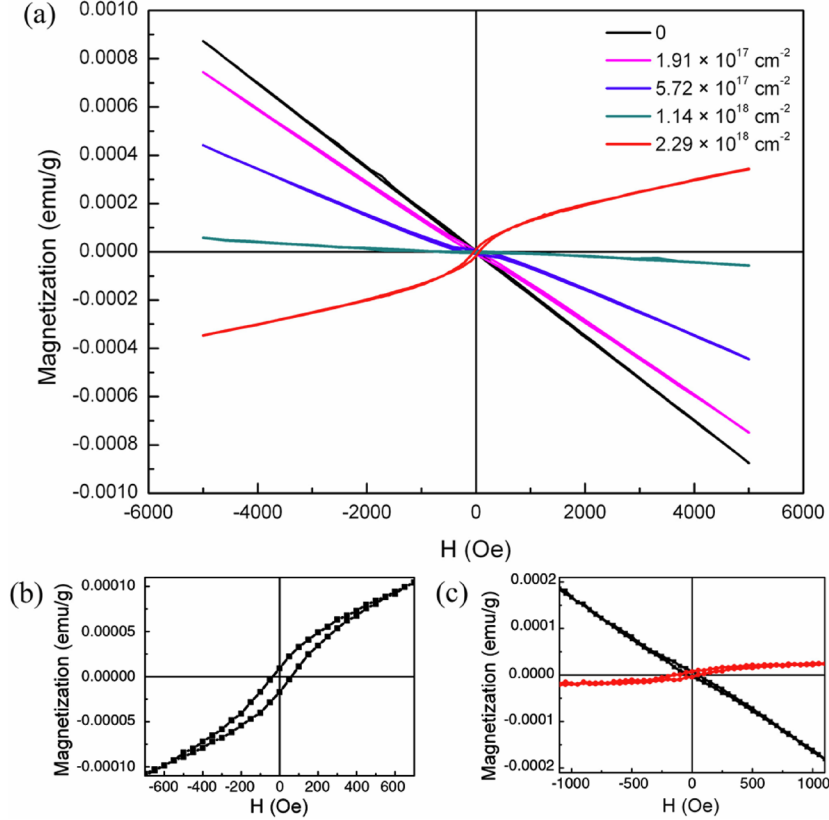


**Figure 8.** (a) The magnetization measured at  $T = 5 \text{ K}$  as a function of magnetic field for neutron-irradiated and pristine 6H-SiC samples. (b) The magnified hysteresis loop for the sample with the fluence of  $2.29 \times 10^{18} \text{ n cm}^{-2}$  at  $T = 5 \text{ K}$ . (c) The magnetic signals with (black) and without (red) the diamagnetic contribution in the low-magnetic field range for the sample with fluence of  $2.29 \times 10^{18} \text{ n cm}^{-2}$  at  $T = 300 \text{ K}$ . Reprinted figure with permission from [48], Copyright 2011 by the American Physical Society.

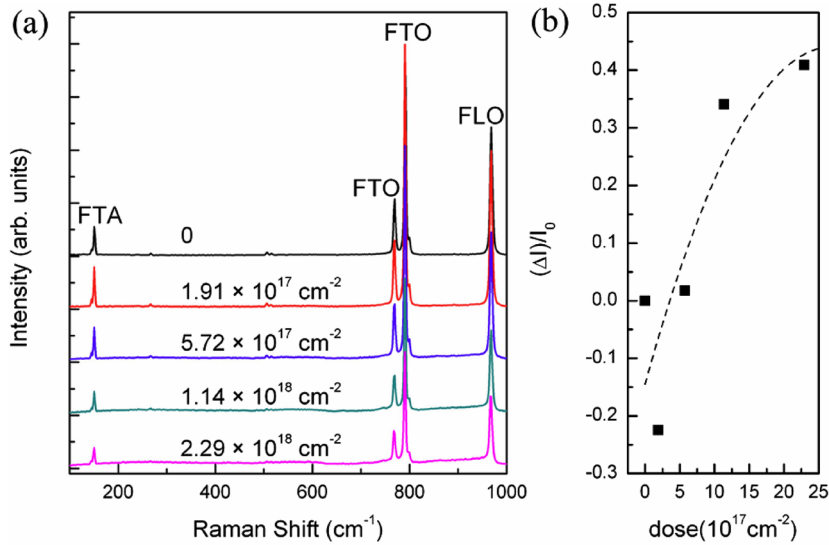


**Figure 9.** (a) Raman spectra from  $100 \text{ cm}^{-1}$  to  $1000 \text{ cm}^{-1}$  for irradiated and pristine 6H-SiC samples. (b) The relative intensity of the folded longitudinal optical mode versus the irradiation fluence. The dashed line is a guide to the eyes. Reprinted figure with permission from [48], Copyright 2011 by the American Physical Society.

corresponds to an essentially damage-free crystal. The minimum yield  $\chi_{min}$ , defined as the ratio of the virgin spectrum to the random spectrum, is 2.3% for the 6H-SiC crystals at the surface region. At the ion fluence of  $5 \times 10^{13}$  or  $1 \times 10^{14} \text{ cm}^{-2}$ , the yield in the channeling spectrum is only slightly higher than in the virgin sample, indicating the detection threshold

of RBS/C. A peak in the channeling spectrum becomes visible for fluences of  $5 \times 10^{14}$  and  $1 \times 10^{15} \text{ cm}^{-2}$ . The damage peak is estimated to occur at a depth of 150 nm, in agreement with SRIM simulations. At the damage peak,  $\chi_{min}$  is calculated to be 5.0%, 8.4%, 33% and 93% for different fluences (dpa). At the same depth,  $\chi_{min}$  is 2.6% for the virgin crystal. Note that for

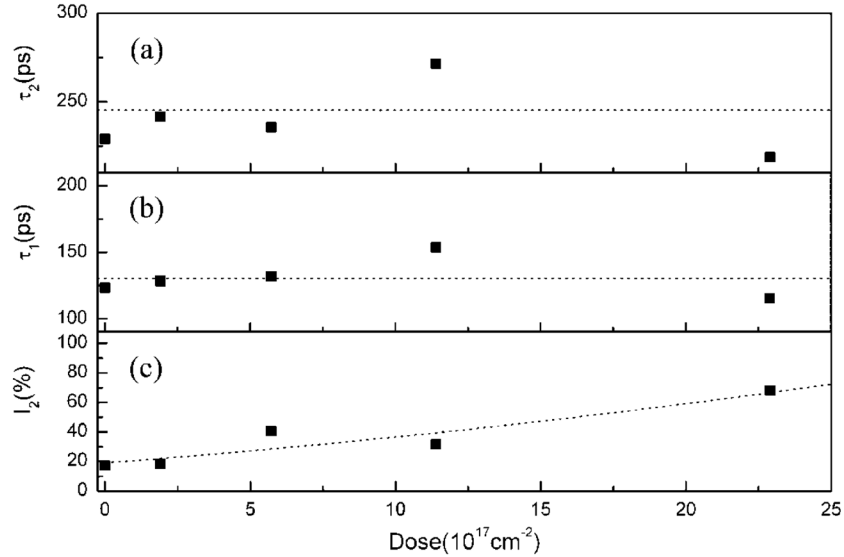


**Figure 10.** Fitted results of  $\tau_2$  (a),  $\tau_1$  (b) and  $I_2$  (c) as functions of the irradiation fluence. Both  $\tau_1$  and  $\tau_2$  are found to be independent of fluence.  $I_2$  is demonstrated to have positive correlation with the fluence. The dotted line shows the average values in (a) and (b); however, it is only a guide to the relationship between  $I_2$  and the irradiation fluence in (c). Reprinted figure with permission from [48], Copyright 2011 by the American Physical Society.

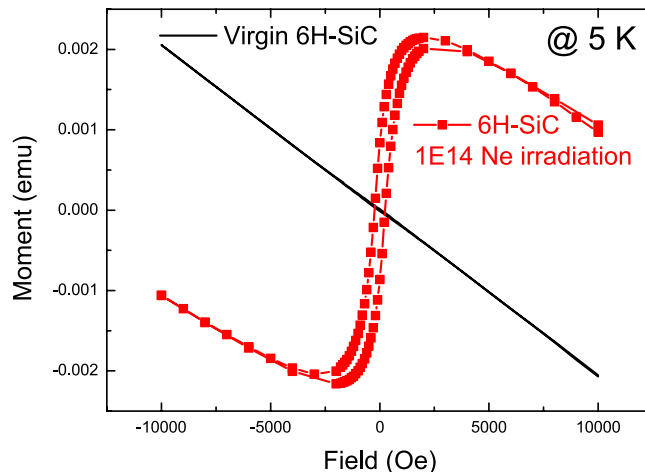


**Figure 11.** Magnetic properties of virgin and ion-irradiated ( $1 \times 10^{14} \text{ cm}^{-2}$ ) 6H-SiC measured at 5 K. Both samples were originally cut from the same wafer. The result has been published in [53].

the fluence of  $1\text{E}15$  (corresponding to the peak *dpa* of around 0.5),  $\chi_{min}$  is 93%, indicating the almost full amorphization at the damage peak. Compared with the magnetization data in figure 12, there is a narrow fluence window, within which the sample is ferromagnetic. The initial introduction of structural disorder leads to pronounced magnetization. Further increasing the disorder induces the amorphization of the host SiC crystal and therefore decreases the saturation magnetization. This is in agreement with the threshold dpa values for amorphization reported in literature [54].

In both papers [48, 53] about ferromagnetism in neutron- and ion-irradiated 6H-SiC, it is tentatively proposed that  $V_{Si}$ - $V_C$  divacancies form local magnetic moments and those local moments ferromagnetically order due to the extended tails of the defect wave functions [48]. As an important technological material, SiC is commercially available at large scales and with

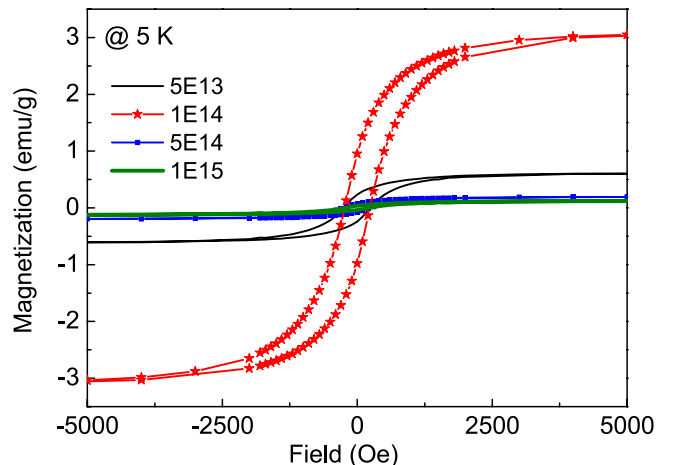


**Figure 12.** Magnetic properties measured at 5 K for 6H-SiC samples with different Ne ion fluences after subtracting the diamagnetic background. All samples were originally cut from the same wafer. The result has been published in [53].

high quality. There are many groups utilizing ions to induce defects and to study magnetic properties in SiC with different polytypes [56–61]. Different defects, such as  $V_{Si}$  [59], are also proposed to be responsible for the ferromagnetism.

### 3.2. Paramagnetism

As shown in figure 8, after neutron irradiation, the diamagnetic background becomes less pronounced. If one checks the field dependence of the magnetization (for the sample with the fluence of  $2.29 \times 10^{18} \text{ n cm}^{-2}$ ), it is like a Brillouin function. In [52], a detailed study over a larger range of neutron irradiation fluence and temperature-dependent magnetization was presented. Samples were commercial semi-insulating 4H-SiC single-crystal wafers from Cree. Particle-induced x-ray emission (PIXE) was performed to check magnetic impurities in

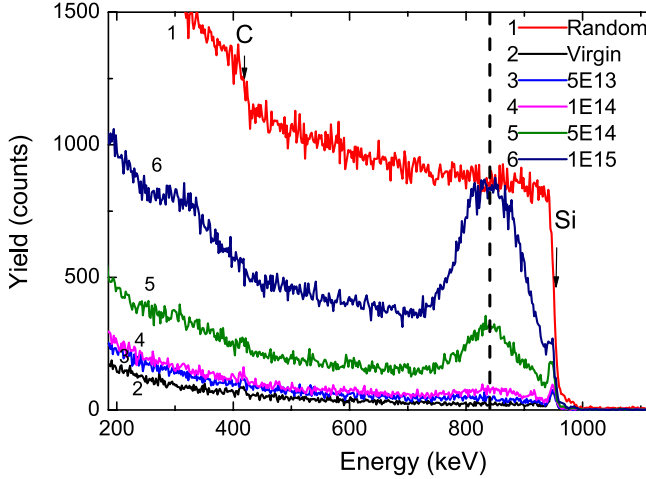


**Figure 13.** A sequence of 1.7 MeV He RBS/C spectra 6H-SiC single crystal implanted with 140 keV Ne ions at room temperature. A random spectrum and a channeling spectrum from a virgin sample are also included for comparison. The dashed line indicates the position of the Si damage peaks. Labels 5E13 to 1E15 indicate the ion fluences, which are  $5 \times 10^{14}$  to  $1 \times 10^{15} \text{ cm}^{-2}$ . Results are partially published in [55].

the pristine sample. The concentrations of magnetic impurities (Fe, Co and Ni) were below the detection limits of about 1 ppm. Neutron irradiation was performed in the DBVK and DBVR chambers at the BER II reactor at Helmholtz-Zentrum Berlin. Since thermal neutrons only produce negligible displacement, only epithermal and fast neutrons were counted in the fluence calculation [30]. The neutron fluence spanned a large range from  $3.28 \times 10^{16} \text{ cm}^{-2}$  to  $3.50 \times 10^{19} \text{ cm}^{-2}$  covering all possibilities from light damage to near amorphization. It is worthy to note that the applied neutron fluence covered the range used in [48] and was extended to much higher fluence values by two orders of magnitude.

Figure 14 shows the magnetic properties measured at 5 K of the virgin 4H-SiC and a sample irradiated with neutrons with a fluence value of  $4.68 \times 10^{17} \text{ cm}^{-2}$ . Here, the results are displayed without any background subtraction but only normalized by the mass of the samples. The difference between the virgin and irradiated SiC is clear to see: the virgin SiC shows purely diamagnetic behavior, while the irradiated one reveals a large deviation from the linear dependence on the magnetic field, which is the contribution from the paramagnetic component. The inset of figure 14 shows the zoom of the low-field part. A ferromagnetic contribution is also induced by neutron irradiation with its saturation magnetization around 1% of the paramagnetic signal.

In order to quantify the paramagnetic centers induced by neutron irradiation, the diamagnetic background has to be carefully subtracted. One can use the diamagnetism measured at higher temperature (here 300 K) for the virgin sample to approximate the diamagnetic background in all samples. Figure 15(a) shows the magnetization ( $M(H)$ ) of neutron-irradiated SiC after subtracting the diamagnetic background. All samples exhibit a paramagnetic component and the magnetization increases with increasing neutron fluence. The paramagnetism can be described by the Brillouin function:

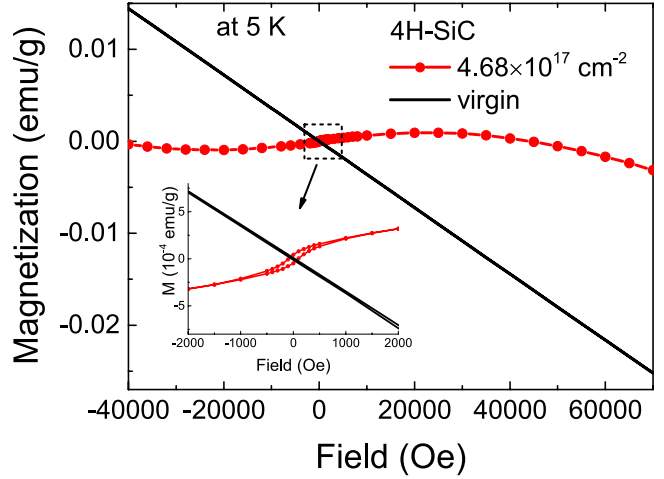


**Figure 14.** Magnetic properties: virgin versus neutron-irradiated 4H-SiC. Inset: the zoom of the low-field range. Reprinted figure with permission from [52], Copyright 2015 by the American Physical Society.

$$M(\alpha) = NJ\mu_B g \left[ \frac{2J+1}{2J} \coth\left(\frac{2J+1}{2J}\alpha\right) - \frac{1}{2J} \coth\left(\frac{\alpha}{2J}\right) \right], \quad (1)$$

where the  $g$  factor is about 2 as obtained from the electron spin resonance measurement [52],  $\mu_B$  is the Bohr magneton,  $\alpha = gJ\mu_B H/k_B T$ ,  $k_B$  is the Boltzmann constant and  $N$  is the density of spins.

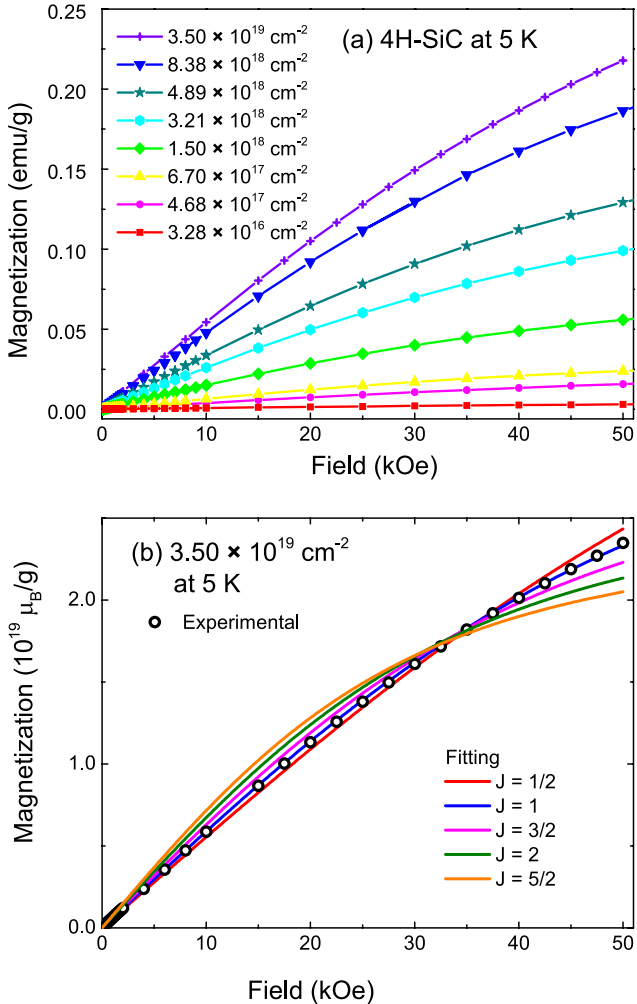
As shown as an example in figure 15(b), the data can be fitted nicely by  $J = 1$ . A larger or smaller  $J$  results in a pronounced deviation from the experimental data. This fitting hints that the measured paramagnetism is due to defects with moment  $\mu = gJ\mu_B = 2\mu_B$ . This conclusion is in excellent agreement with our first-principles calculation (shown in section 3.4): the induced magnetism is due to  $V_{Si}-V_C$  divacancies which carry a magnetic moment of  $2\mu_B$ . As a comparison, the induced magnetism in graphite is generally attributed to single vacancy [62–65].

Figure 16 presents the temperature-dependent magnetization ( $M(T)$ ) for samples with different neutron fluences under an applied field of 10 000 Oe. The diamagnetic background is essentially temperature-independent and therefore dominates at higher temperature. The Curie-like paramagnetic component shows a strong dependence on temperature and neutron fluence. Self-consistently, the  $M(T)$  curves can be well fitted according to the Curie law (equation 2) by using the same  $J$  and  $N$  obtained from the corresponding  $M(H)$  curve fitting:  $J = 1$  and  $N = 1.66 \times 10^{19} \text{ g}^{-1}$  for the sample shown in figures 15(b) and 16(b).

$$\chi = \frac{M}{H} = N \frac{J(J+1)(g\mu_B)^2}{3k_B T}. \quad (2)$$

It has been shown that thermal annealing can partially heal the induced defects. The removal of defects is reflected by the magnetization measurements. As shown in figure 17, the magnetization of irradiated SiC is reduced gradually after thermal annealing at different temperatures.

The paramagnetism in defective SiC was also revealed in nanocrystalline SiC [66]. The magnetization of the films is correlated with the deposition temperature. At higher deposition



**Figure 15.** (a) Magnetization of neutron-irradiated samples measured at 5 K as a function of field ( $M(H)$ ). The numbers label the neutron fluences. The diamagnetic background has been subtracted. (b) Fits of the magnetization measured at 5 K for the sample with a fluence of  $3.50 \times 10^{19} \text{ cm}^{-2}$  using the Brillouin function with different values of  $J$ . Reprinted figure with permission from [52], Copyright 2015 by the American Physical Society.

temperature, the magnetization becomes lower. The authors concluded that the magnetism in nanocrystalline SiC films is from neutral charged  $\text{V}_{\text{Si}}\text{-}\text{V}_C$  divacancies.

### 3.3. Magnetic phases in ion-irradiated SiC

As shown in the preceding two sections, both paramagnetism and ferromagnetism can be detected in defective SiC. In principle, paramagnetism or the appearance of local moments is the prerequisite for ferromagnetism (the result of interaction between local moments). Therefore, in ion-irradiated SiC, in which the defects are not uniformly distributed, there should be mixed magnetic phases including paramagnetism and ferromagnetism. However, paramagnetism is weak and difficult to detect.

A careful analysis was done for Ne-irradiated 6H-SiC [67]. Figure 18(a) shows the comparison of the hysteresis loops measured at 5 K for virgin SiC and for sample 1E14. The implantation energy was 140 keV and the sample label

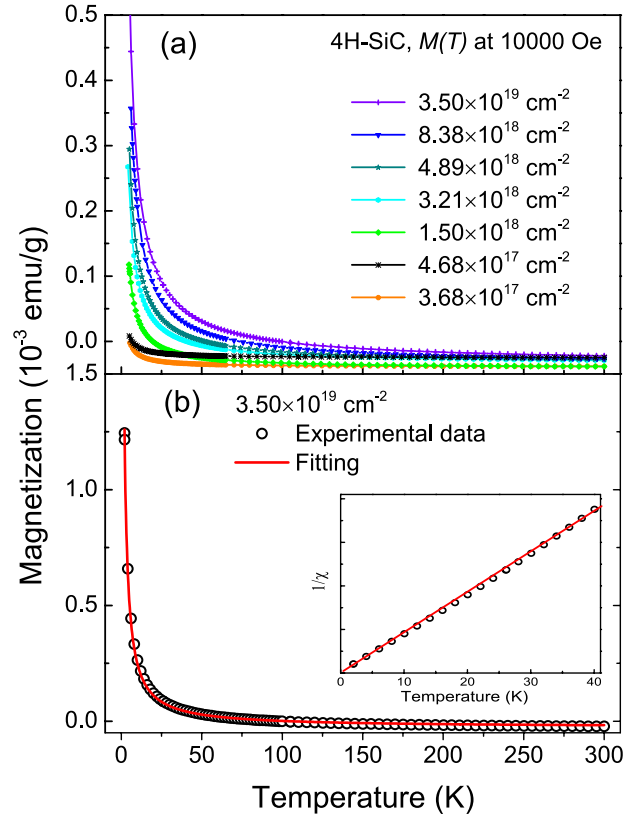


**Figure 16.** (a) The magnetic moment of neutron-irradiated 4H-SiC samples measured under a magnetic field of 10000 Oe as a function of temperature ( $M(T)$ ). The numbers label the neutron fluences. (b) Fitting by equation (2) for the sample irradiated with the largest fluence: the black symbols are experimental data and the red solid curve is the fitting result. Reprinted figure with permission from [52], Copyright 2015 by the American Physical Society.

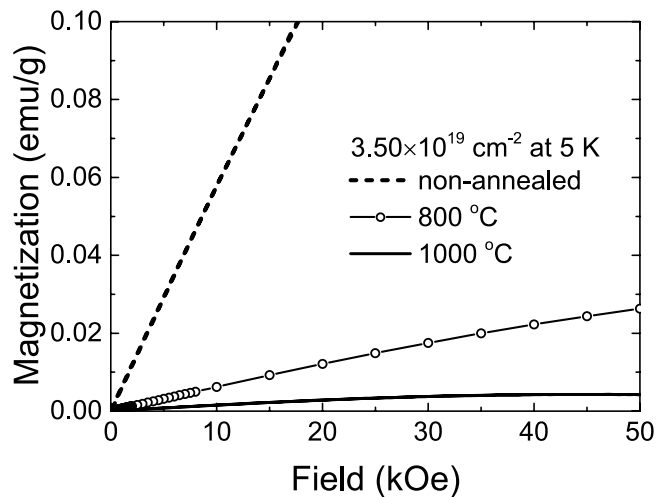


**Figure 17.** Magnetization of irradiated 4H-SiC after annealing at different temperatures: measurements at 5 K as a function of field ( $M(H)$ ). Adapted figure with permission from [52], Copyright 2015 by the American Physical Society.

1E14 means the ion fluence of  $1 \times 10^{14} \text{ cm}^{-2}$ . In figure 18(b), we display the magnetization of sample 1E14 after removing the diamagnetism and the paramagnetism from the substrate. After this treatment, the paramagnetic part can be mostly subtracted, but not completely. The slightly increased

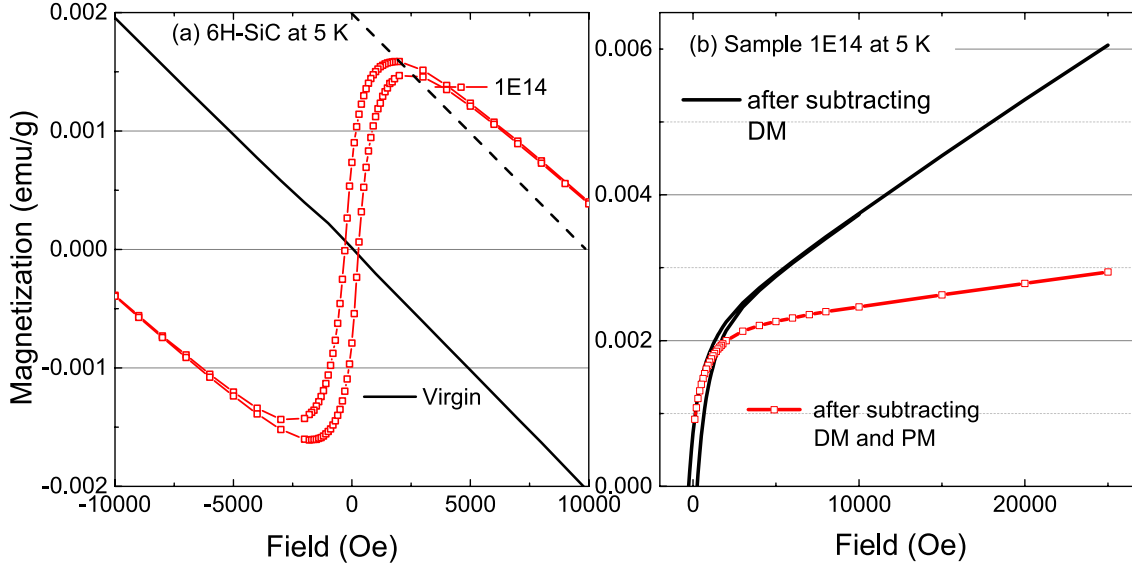


**Figure 18.** (a) The hysteresis loops measured at 5 K for the virgin 6H-SiC (single crystal) and sample 1E14. The dashed line is a guide for the eye to show the diamagnetic background from the substrate. (b) Magnetization at 5 K of sample 1E14 after subtracting different contributions from the substrate. DM: diamagnetism, and PM: paramagnetism. The magnetization is normalized by the whole sample mass. To subtract the PM contribution, only 1/4 of the hysteresis data were numerically processed. Adapted figure with permission from [67], Copyright 2014 by the American Physical Society.

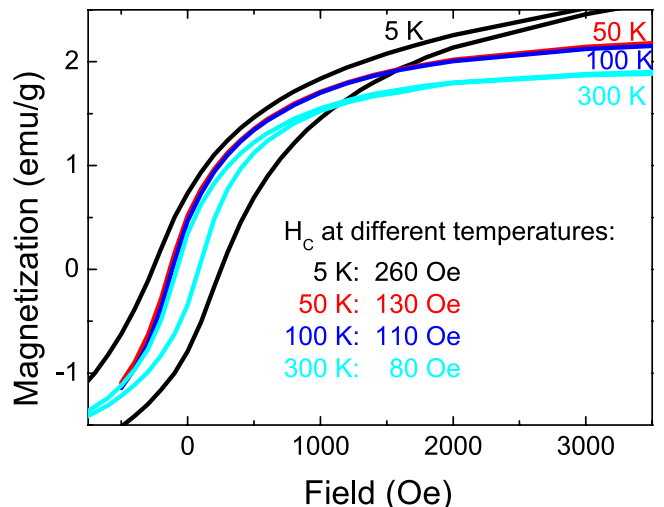
magnetization with field at the large-field part (shown in figure 18(b)) indicates a paramagnetic contribution in the irradiated sample.

Figure 19 shows the hysteresis loops of sample 1E14 measured at different temperatures. One can observe three features: (1) the hysteresis persists above room temperature, (2) there is only a slight decrease of the saturation magnetization, and (3) the coercivity changes at different temperature range. The coercivity drops from 260 Oe at 5 K to 130 Oe at 50 K, and then drops slowly with increasing temperatures. These features indicate the co-existence of ferromagnetism and superparamagnetism [68–70].

It is unrealistic to calculate separate hysteresis loops for the ferromagnetic and superparamagnetic components. But the magnetic remanence and coercivity for the superparamagnetic component show different behavior compared with ferromagnetism upon increasing temperature. Therefore, one can analyze the temperature-dependent magnetic remanence to decompose it into different components as shown in figure 20. For superparamagnetism, the remanence and coercivity are more sensitive to temperature [69]. As shown in figure 20, the magnetic remanence measured at 10 Oe (a small field to compensate the possible trapped field in the superconductor magnet of the measurement setup) shows two distinct regimes with increasing temperature: it decreases rapidly below 50 K and moderately above 50 K. This is consistent with the coercivity change with increasing temperature shown in figure 19. The temperature dependence of magnetization for superparamagnetism and single-phase ferromagnetism can be described by their sum [71]:

$$M = M_s(0)[1 - (T/T_c)^{3/2}] + n\mu[\coth(\mu H/k_B T) - k_B T/\mu H]. \quad (3)$$

The first term represents the spontaneous magnetization of the ferromagnetic component at temperatures below the Curie



**Figure 19.** Hysteresis loops at different temperatures for sample 1E14 (single-crystalline 6H-SiC). Note that only a half loop was measured at temperatures 50 and 100 K. One can see a fast drop of the coercivity from 5 K to 50 K, but a slower decrease above 50 K. The magnetization is normalized by the mass of the implanted layer corresponding to around 0.1% of the sample. Reprinted figure with permission from [67], Copyright 2014 by the American Physical Society.

temperature and the second refers to the superparamagnetism. For the first term,  $T_C$  is the Curie temperature,  $M_s(0)$  is the spontaneous magnetization at 0 K, and  $k_B$  is the Boltzmann constant. For the second term,  $n$  is the density of superparamagnetic clusters and  $\mu$  is the average magnetic moment of one superparamagnetic cluster.

As shown in figure 20, the temperature-dependent magnetization can be well fitted by considering both superparamagnetism and ferromagnetism contributions. For

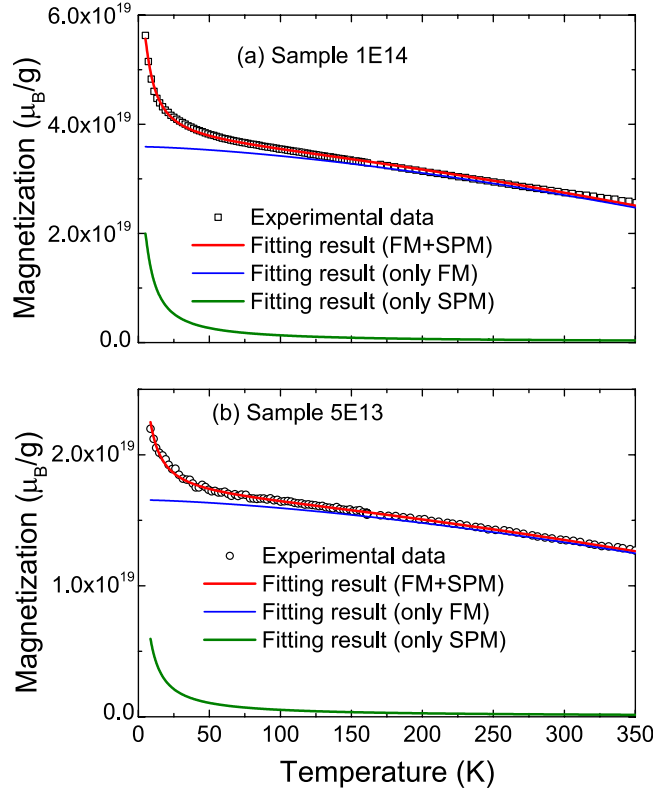


**Figure 20.** Magnetic remanence of Ne-irradiated 6H-SiC samples: one can see the large difference of the magnetization versus temperature at temperatures below and above 50 K. The data are shown without considering the diamagnetic and paramagnetic background which is negligible due to the small field. The solid lines are fits according to equation (3). Reprinted figure with permission from [67], Copyright 2014 by the American Physical Society.

superparamagnetism the spontaneous magnetization can only appear below the blocking temperature. For both samples, the contribution from the superparamagnetic component drops to zero at temperatures slightly above 50 K. For sample 1E14, the fitting results show that one superparamagnetic cluster contains around  $8.1 \times 10^4 \mu_B$ . According to the theoretical calculation [48], each divacancy generates  $2 \mu_B$ . Assuming the magnetic moments arising from  $V_{Si}V_C$  divacancies, one magnetic cluster in sample 1E14 contains around 40 000  $V_{Si}V_C$  divacancies; however, it is difficult to correlate it to a physical cluster size. For the ferromagnetic contribution, the best fitting gives  $T_C$  of around 760 K. Although the saturation magnetization is different for samples 5E13 and 1E14 (see figure 18), both samples show a similar behavior in the temperature-dependent magnetic remanence. The ferromagnetic component of sample 5E13 is deduced to also have a  $T_C$  around 750 K, implying that the magnetic properties in both ion-irradiated SiC samples have the same origin.

The coexistence of different magnetic phases can also be concluded by the ZFC/FC measurements as shown in figure 21. The ZFC magnetization was measured by cooling the sample from 300 K to 5 K under zero field, then a field of 100 Oe was applied and the magnetization was measured during warming up. The FC curves were measured by cooling the sample in a field of 10 000 Oe, then at 5 K the field was decreased to

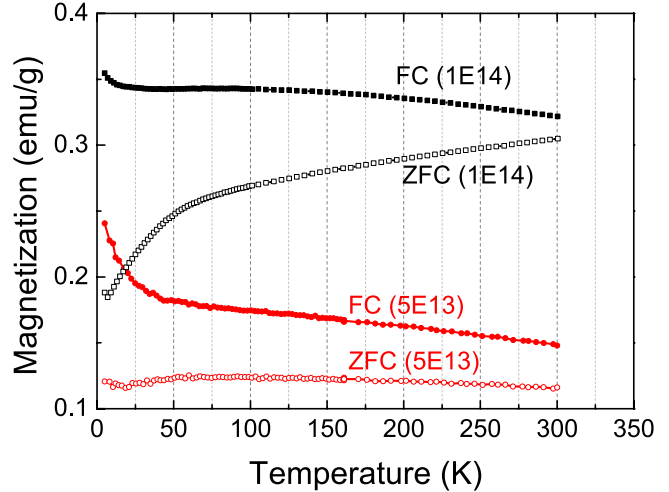


**Figure 21.** ZFC/FC magnetization for two irradiated 6H-SiC samples with Ne ion fluences of  $5 \times 10^{13} \text{ cm}^{-2}$  (5E13) and  $1 \times 10^{14} \text{ cm}^{-2}$  (1E14), respectively. Thermal irreversibility has been observed for both samples. The data are shown without subtracting the diamagnetic and paramagnetic background which is negligible at the applied small field. Reprinted figure with permission from [67], Copyright 2014 by the American Physical Society.

100 Oe and the magnetization was measured also during warming up. The ZFC/FC curves for both samples are different from those of samples with a single magnetic phase. For a superparamagnetic system (e.g. magnetic nanoparticles) the ZFC curve would increase with temperature, peak at a particular temperature range and finally merge with the FC magnetization. For a ferromagnetic system, when the coercivity is larger than the applied field, the ZFC magnetization can be very small compared with the FC magnetization and temperature-independent below the Curie temperature. When the coercivity is small, the ZFC curves superimpose on the FC curves [72]. For both SiC samples shown in figure 21, the ZFC/FC curves cannot be explained by a single magnetic phase. They can only be understood if assuming a superparamagnetic phase with blocking temperature around 50 K and a ferromagnetic phase with Curie temperature well above 300 K.

To understand the co-existence of paramagnetism, superparamagnetism and ferromagnetism in ion-irradiated SiC, we can consider the following facts: (1) the defects in SiC are non-homogeneously distributed, (2) the isolated, uncoupled defects contribute to the paramagnetism, and (3) the coupled defects result in the superparamagnetic and ferromagnetic components. The ferromagnetic coupling is expected to first appear within regions with proper defect concentrations. Some regions are connected to be big enough and behave as a ferromagnet. Some regions with ferromagnetically coupled defects are small and behave as superparamagnets. In a recent work on Gd-doped GaN [73], Thiess *et al* found that intrinsically the Ga vacancies tend to cluster, leading to the co-existence of ferromagnetism and superparamagnetism. This scenario could also explain the experimental results in ion-irradiated SiC.

Such a co-existence of different magnetic phases including paramagnetic, superparamagnetic and ferromagnetic components has been also identified in nano-crystalline SiC with

defects [66], in reduced graphene oxide [74] and in irradiated graphite [75, 76].

### 3.4. Coupling mechanism (first-principles calculations)

To understand the formation of local moments and the magnetic coupling between them, first-principles calculations are indispensable. One early attempt has been done for 3C-SiC. In [77], the author addressed the interactions between Si vacancies  $V_{Si}$  in 3C-SiC. High-spin configurations are predicted for the negatively-charged  $V_{Si}$  defects. Ferromagnetic coupling is possible when  $V_{Si}$  defects are at  $-2e$  charge state, while  $V_{Si}$  defects at  $-e$  charge state tend to order antiferromagnetically. The authors proposed to use nitrogen doping to manipulate the charge states of  $V_{Si}$  and thereby the magnetic interactions between them. When the N: $V_{Si}$  ratio is near 1:1,  $V_{Si}$  is at the high-spin ground state with a local magnetic moment of  $3 \mu_B$  and the states interact with each other antiferromagnetically. When the N: $V_{Si}$  ratio is around 2:1,  $V_{Si}$ -induced local magnetic moments are  $2 \mu_B$  per vacancy and they couple ferromagnetically. N-ion implantation was done experimentally for 6H-SiC [59]. Both ferromagnetism and  $V_{Si}$  were detected in the sample, supporting the first-principles calculations. However, in another work, N implantation induced much weaker magnetism than Al implantation in 4H-SiC [78].

For neutron-irradiated 6H-SiC [48],  $V_{Si}$ - $V_C$  divacancies were identified. First-principles calculations revealed that  $V_{Si}$ - $V_C$  divacancies can lead the formation of local moments and the extended tails of defect wave functions make long-range ferromagnetic coupling possible. The calculated spin-resolved density of states (DOS) of the 192-atom supercell (see figure 22(a)) shows that each neutral axial ( $hh$ )  $V_{Si}$ - $V_C$  yields a magnetic moment of  $2.0 \mu_B$ . The spin-polarization energy, the energy difference between the spin-polarized and spin-unpolarized states, was calculated to be  $1.90 \text{ eV}$ , meaning that the spin-polarized state is stable well above room temperature. The spin polarization induced by the neutral  $V_{Si}$ - $V_C$  leads to a  $0.50 \text{ eV}$  splitting between the majority and minority spin states. Figure 22(b) shows the charge density isosurface of defect states associated with a neutral  $V_{Si}$ - $V_C$  in the 192-atom supercell. It demonstrates both the localized nature and the extended tails of the defect wave functions beyond the supercell.

If doubling the size of the supercell by putting two 192-atom cells side by side, one can estimate the magnetic coupling (ferromagnetic or antiferromagnetic) between the  $V_{Si}$ - $V_C$ -induced local moments. The energy difference between the antiferromagnetic and ferromagnetic phases is  $E_{AFM} - E_{FM} = 8J_0S^2$  according to the nearest-neighbor Heisenberg model, where  $J_0$  is the nearest-neighbor magnetic coupling and  $S$  is the net spin of the defect states. A negative  $J_0$  means that antiferromagnetism is energetically favored and otherwise ferromagnetism is favored. The calculation results show that when the divacancies  $V_{Si}$ - $V_C$  in 6H-SiC are separated by  $12.3 \text{ \AA}$ ,  $J_0$  is  $-9.8 \text{ meV}$  for a neutral charge  $(0, 0)$  state,  $8.4 \text{ meV}$  for  $(+1, +1)$  and  $34.1 \text{ meV}$  for  $(-1, -1)$  charge states.

To investigate how the spin-polarization energy and  $J_0$  depend on the defect concentration, more detailed calculations

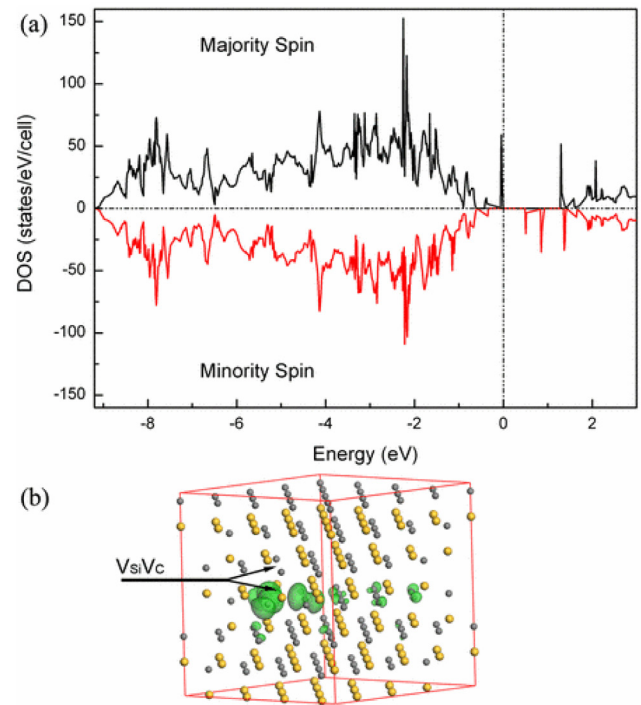


**Figure 22.** (a) Spin-resolved DOS of a neutral axial ( $hh$ )  $V_{Si}$ - $V_C$  in a 192-atom 6H-SiC supercell. The spin polarization leads to a splitting between two kinds of spin states. (b) Isosurface charge density plot (the isovalue is  $0.02 \text{ e A}^{-3}$ ) of the total spin states about a neutral  $V_{Si}$ - $V_C$  in a 192-atom SiC supercell, showing both the localized nature and the extended tails of the defect wave functions. Si atoms are shown in yellow and C atoms in gray. Arrows indicate the location of  $V_{Si}$ - $V_C$ . Reprinted figure with permission from [48], Copyright 2011 by the American Physical Society.

have been done for 4H-SiC [52]. The spin-polarizing energies  $\Delta E_{sp}$  of supercells as a function of  $d_V$  are shown in figure 23.  $d_V$  is defined as the distance between adjacent axial ( $hh$ )  $V_{Si}$ - $V_C$  in the  $a$ - $b$  plane. It is found that  $\Delta E_{sp}$  increases when  $d_V$  increases, indicating that the spin polarization is more stable under low  $V_{Si}$ - $V_C$  concentrations. When  $d_V$  is larger than  $9.7 \text{ \AA}$ ,  $\Delta E_{sp}$  changes from negative to positive and the spin polarization becomes energetically favored. Here, the supercells with  $d_V$  less than  $9.7 \text{ \AA}$  are designed to obtain the critical value of  $d_V$  switching the sign of  $\Delta E_{sp}$ . Besides, each  $V_{Si}$ - $V_C$  yields a local moment of  $2.0 \mu_B$  when  $d_V$  is more than  $12.34 \text{ \AA}$ . This result is in good agreement with the experimental data shown in figures 15 and 16. The experimental results show that the induced paramagnetism is due to a single species with moment of  $2 \mu_B$ .

Table 2 displays the calculated  $J_0$  for different  $d_V$  and charge states.  $V_{Si}$ - $V_C$  does not couple with each other along the  $c$  axis, even when  $d_V$  is as small as  $10.11 \text{ \AA}$ . The exchange interaction is much stronger along the  $a$  axis and strongly depends on the charge state. Neutron or positively charged  $V_{Si}$ - $V_C$  antiferromagnetically couples with a maximal exchange interaction of  $125.68 \text{ meV}$  when  $d_V$  is  $12.33 \text{ \AA}$ . Negatively charged  $V_{Si}$ - $V_C$  divacancies favor a ferromagnetic coupling. However, the exchange interaction dramatically decreases from  $49.36 \text{ meV}$  to  $3.71 \text{ meV}$  when  $d_V$  is increased from  $12.33$  to  $18.50 \text{ \AA}$ .

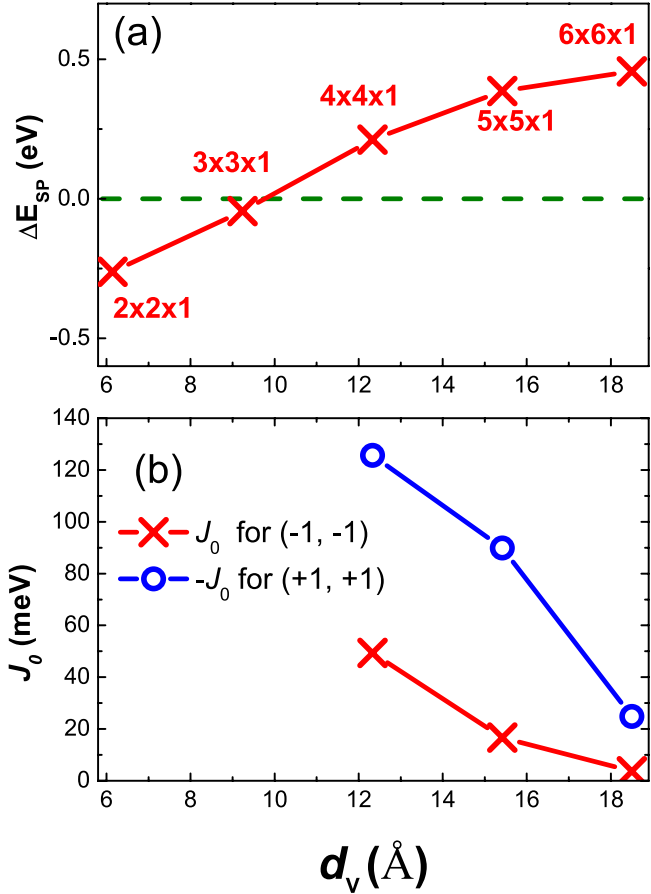


**Figure 23.** (a) Spin-polarization energy  $\Delta E_{sp}$  as a function of the distance  $d_V$  between the adjacent axial ( $hh$ ) divacancies in 4H-SiC.  $\Delta E_{sp}$  increases with increasing  $d_V$  and the critical value is 9.7 Å. The corresponding supercell structures with one  $V_{Si}-V_C$  are marked with the numbers and multiplication signs. (b) The ferromagnetic (or antiferromagnetic) exchange coupling energy between charged  $(-1, -1)$  or  $(+1, +1)$  divacancies as a function of  $d_V$ . Reprinted figure with permission from [52], Copyright 2015 by the American Physical Society.

**Table 2.** Magnetic coupling between axial ( $hh$ )  $V_{Si}-V_C$ -induced local moments in 4H-SiC. The coupling is antiferromagnetic between neutral or positively charged  $V_{Si}-V_C$  while ferromagnetic between negatively charged ones. When the alignment direction of  $V_{Si}-V_C$  is along the  $c$  axis, the coupling almost does not exist. Results are from [52].

$d_V$ (Å)	$c$ - or $a$ axis	Charge state	$E_{AFM}-E_{FM}$ (meV)	$J_0$ (meV)
10.11	$c$ axis	(0, 0)	-0.55	-0.14
12.33	$a$ axis	(0, 0)	-39.45	-4.93
12.33	$a$ axis	(+1, +1)	-251.35	-125.68
12.33	$a$ axis	(-1, -1)	98.73	49.36
15.42	$a$ axis	(0, 0)	-5.77	-0.72
15.42	$a$ axis	(+1, +1)	-179.81	-89.90
15.42	$a$ axis	(-1, -1)	33.31	16.66
18.50	$a$ axis	(0, 0)	-0.93	-0.12
18.50	$a$ axis	(+1, +1)	-49.75	-24.88
18.50	$a$ axis	(-1, -1)	7.43	3.71

In figure 23(b), we plot the ferromagnetic exchange interaction energy as a function of  $d_V$ . As shown in figures 23(a) and (b), the ferromagnetism induced by divacancies requires that divacancies are negatively charged with  $d_V$  in the range from 12.33 Å to 15.42 Å. The required  $d_V$  would correspond to a concentration of divacancies in the order of  $3-6 \times 10^{20} \text{ cm}^{-3}$  ( $1/d_V^3$ ). This concentration is well above the maximum concentration for the local moments obtained by neutron irradiation [52]. However, after irradiation with the largest neutron fluence the sample is approaching amorphous and the density of paramagnetic centers ( $N$ ) starts to saturate. In this sense, it is unrealistic to expect ferromagnetic coupling throughout the whole bulk sample. The experimentally observed weak ferromagnetism can be understood as a local effect: only some regions with nm or  $\mu\text{m}$  dimension can accommodate a high concentration of divacancies. These regions form ferromagnetic bubbles with very strong interaction (see table 2), leading to the high Curie temperature. Presumably, these regions could be a surface, interface or grain boundary. However, according to our calculation the spin polarization will be unfavorable if  $d_V$  is too small. Therefore, the narrow fluence window of ferromagnetism shown in neutron-irradiated SiC [52] as well as in neon-implanted SiC [53] can be understood: for samples irradiated with low fluences, some local regions accommodating a larger concentration of divacancies appear to be ferromagnetic. When  $d_V$  in the local regions reaches the critical value of 9.7 Å, the increase of irradiation fluence (defect concentration) will suppress the spin polarization. There may appear some new local regions with the concentration of divacancies reaching the level to induce ferromagnetism, but the damage to the crystalline structure by irradiation will weaken the coupling. Therefore, the amount of paramagnetic centers can be scaled up with neutron fluence and shows saturation at very large fluences.

For SiC nanostructures, the situation can be different. Morbec *et al* investigated the effects of vacancies on the magnetic properties of zigzag SiC nanoribbons (Z-SiCNR) using *ab initio* calculations based on density functional theory [79]. Single ( $V_C$  and  $V_{Si}$ ) and double ( $V_{Si}V_{Si}$  and  $V_{Si}-V_C$ ) vacancies were found to induce magnetism in Z-SiCNRs. A single  $V_C$  can lead to a transition from half-metallic to metallic behavior in Z-SiCNRs due to the edge Si  $p$ -orbitals and the atoms surrounding the vacancy. Foreign impurity atoms (B and N) can interact with vacancies. The formation energies of vacancies can be reduced by substitutional B and N atoms. Ferromagnetism can be expected if Z-SiCNRs are grown under proper conditions.

### 3.5. Microscopic origin

In the previous sections, we have shown that divacancies  $V_{Si}-V_C$  are the dominating defect type in neutron- and ion-irradiated SiC. Note that the nearest-neighbor atoms of  $V_{Si}-V_C$  include three carbon atoms as well as three silicon atoms. It is therefore interesting to clarify where the local moments reside. XANES and x-ray magnetic circular dichroism (XMCD) are element-specific techniques and have been used

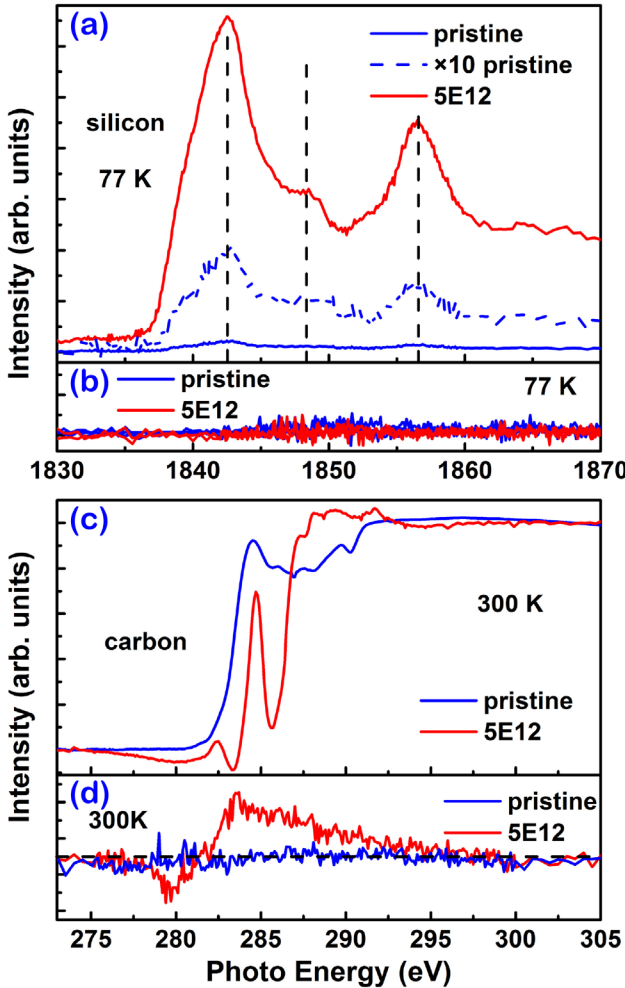


**Figure 24.** X-ray absorption spectra measured in electron yield mode for the sample 5E12 (the Xe irradiation fluence  $5 \times 10^{12} \text{ cm}^{-2}$ ) and the pristine 6H-SiC sample: (a) XANES at the silicon K-edge at 77 K, (b) XMCD at the silicon K-edge at 77 K, (c) XANES at the carbon K-edge at 300 K, (d) XMCD at the carbon K-edge at 300 K. Reproduced from [50]. CC BY 4.0.

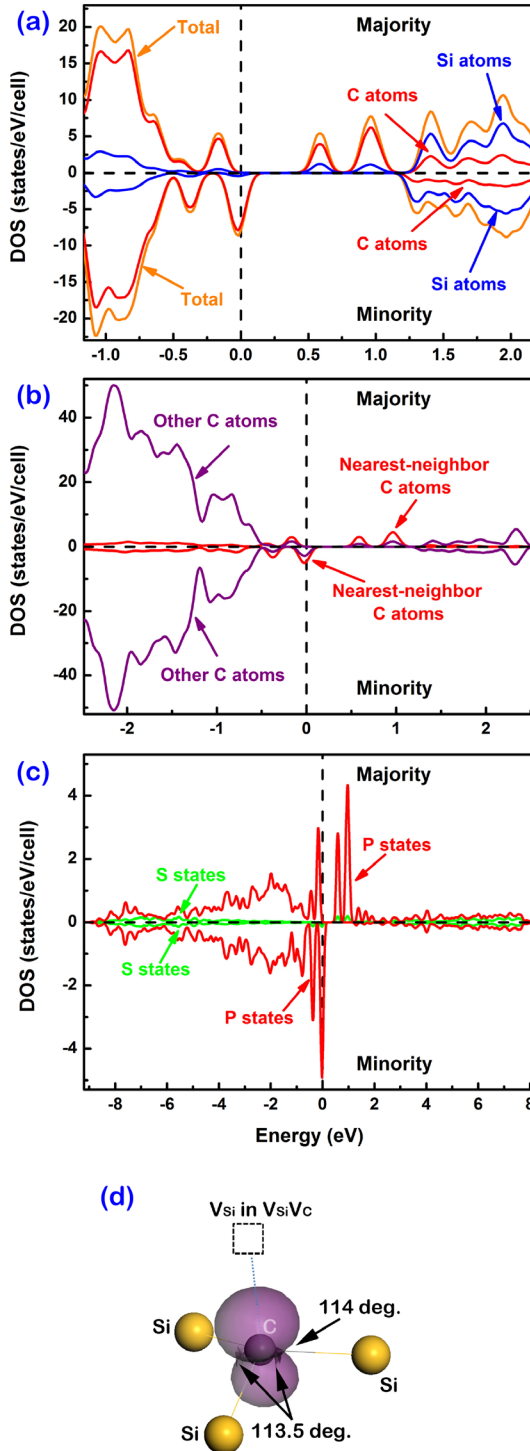
to measure the magnetic contribution from different elements with partially occupied  $3d$  or  $4f$  subshells [80, 81]. Ohldag *et al* [82] applied XMCD to investigate the magnetism at the carbon K-edge in proton-irradiated highly oriented pyrolytic graphite. XANES was used to investigate the bonding state in SiC single crystals [83]. Therefore, it is possible to understand the microscopic picture of the defect-induced ferromagnetism in SiC using soft x-ray spectroscopy.

Figure 24(a) shows the XANES spectra of the silicon K-edge for 6H-SiC. Comparing with the pristine sample, the peak positions of irradiated samples are not changed, but the relative strength of the peak at 1848 eV decreases, which suggests an increase of defect density [83]. As shown in figure 24(b), the XMCD signal is within the detection noise level in both the pristine sample and the sample 5E12 (the sample was implanted with Xe ions at 500 keV to a fluence  $5 \times 10^{12} \text{ cm}^{-2}$ ) at the silicon K-edge. No spin-polarized states close to the Fermi level occur at silicon atoms, and thus silicon centers do not contribute to the ferromagnetism observed in sample 5E12. Figure 24(c) shows the XANES spectra at the carbon

K-edge of sample 5E12 and the pristine sample measured at 300 K. Resonances around 285 eV and 290 eV are attributed to the transition of carbon  $1s$  core-level electrons to  $\pi^*$  and  $\sigma^*$  bands, respectively [82]. The resonance at 285 eV of the sample 5E12 is sharper than that of the pristine sample. The orbital hybridization in carbon is modified from the diamond-like  $sp^3$ -type carbon in pure 6H-SiC towards a more planar, graphitic  $sp^2$ -type carbon center, which leaves the orthogonal  $p_z$  orbital unchanged and gives rise to the peak of  $\pi^*$  bands [84]. This feature indicates a change of the local coordination from the tetrahedrally coordinated carbon atom in pristine SiC to the three-fold bound carbon site. In sharp contrast to the silicon K-edge, a sizeable XMCD signal appears at the carbon K-edge as shown in figure 24(d). Therefore, we can conclude that the defect-induced ferromagnetism originates from a spin-polarized partial occupancy of the  $p_z$  orbitals at carbon atoms close to defect sites in SiC.

In [50], first-principles calculations were employed to understand why the magnetic signal was observed only from carbon atoms. As shown in figure 25(a), 90% of the spin polarization is contributed by the valence states of the carbon atoms. This explains why XMCD is only observed at the carbon K-edge. Further, by comparing the partial spin-resolved DOS of nearest-neighbor carbon atoms with that of other carbon atoms, it is visible that 85% of magnetic moments are from the three nearest-neighbor carbon atoms (see figure 25(b)). Therefore the magnetic moments of the nearest-neighbor carbon atoms of  $V_{Si}-V_C$  are mainly responsible for the ferromagnetism. In SiC, carbon has higher electronegativity than silicon, and unpaired electrons will thus have a tendency to be attracted by carbon atoms. Spin polarization thus mainly appears at those carbon atoms around the vacancies. As shown in figure 25(c), our calculation indicates that most of the magnetic moments (90%) originate from the  $p$  states of nearest-neighbor carbon atoms of  $V_{Si}-V_C$ . Due to the attraction of the remaining adjacent silicon atoms, the nearest-neighbor carbon atoms will move away slightly from the  $V_{Si}-V_C$  divacancies. This structure change from the unperturbed four-fold bulk coordination to a more planar three-fold bound state is connected with rehybridizations at those C atoms in the close vicinity of  $V_{Si}-V_C$ . The distortion will modify the electronic structure locally towards a higher degree of  $sp^2$  bonding orbitals and a singly occupied  $p$ -type lone pair at the C atoms. Thus, their outermost orbitals will acquire a significant  $\pi$  character and the magnetic moments are mainly contributed by  $p$  electrons, as shown in figure 25(d). The first-principles calculations corroborate the interpretation of the XMCD experiment well: the XMCD signal of SiC after irradiation is thus assigned to  $p$  electrons.

In another work, electron magnetic circular dichroism (EMCD) was used to measure the atomic origin of ferromagnetism in Al-doped 4H-SiC [85]. EMCD was performed in transmission electron microscopy, measuring the difference in core-level electron energy loss spectra collected at two opposite chirality conditions. As with XMCD, EMCD can detect the magnetic moments of a particular element. In the work by He *et al* [85], EMCD signals were observed in C atoms in



**Figure 25.** The electronic structure of  $\text{Si}_{95}(\text{V}_{\text{Si}})\text{C}_{95}(\text{V}_C)$  (6H-SiC): (a) The total spin-resolved DOS and the partial spin-resolved DOS of silicon atoms and carbon atoms, respectively. (b) Comparison of partial spin-resolved DOS of nearest-neighbor carbon atoms and others. (c) Comparison of the partial spin-resolved DOS of  $s$  and  $p$  electrons of nearest-neighbor carbon atoms of  $\text{V}_{\text{Si}}-\text{V}_C$ . (d) The structure and spin density isosurface ( $0.08 \text{ e } \text{\AA}^{-3}$ , in purple) around one of the nearest-neighbor carbon atoms. The carbon atom is in dark purple in the middle and silicon atoms are in yellow. The arrows indicate the bond angles of  $\text{Si}-\text{C}-\text{Si}$ . The dashed line and square symbol indicate the direction and the location of the adjacent silicon vacancy part ( $\text{V}_{\text{Si}}$ ) within axial ( $hh$ )  $\text{V}_{\text{Si}}-\text{V}_C$ , respectively. The vertical dashed lines at zero indicate the Fermi energy. Reproduced from [50]. CC BY 4.0.

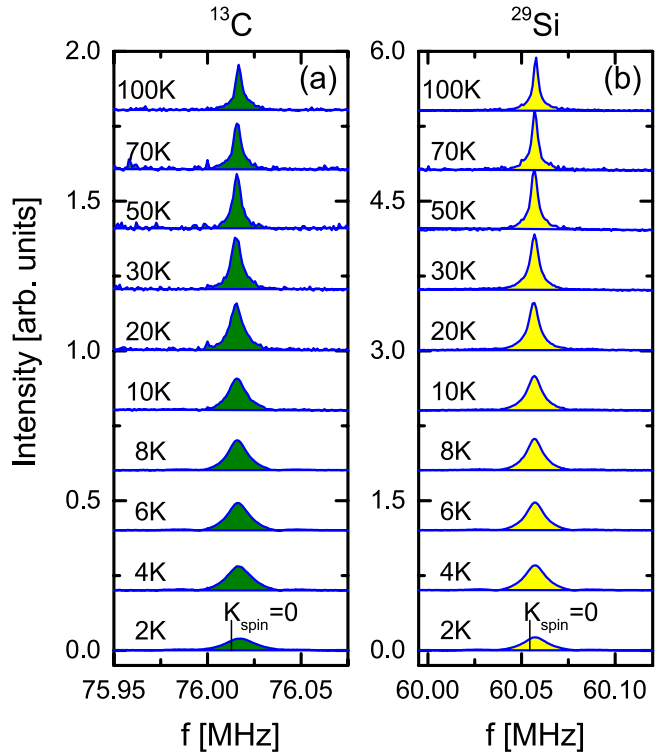


**Figure 26.** Experimental (a)  $^{13}\text{C}$  and (b)  $^{29}\text{Si}$  NMR spectra for the neutron-irradiated 6H-SiC sample at different temperatures at a magnetic field of  $\mu_0 H = 7.100 \text{ T}$ . The vertical markers over the spectra at 2 K label the frequency where  $K_{\text{spin}} = 0$ . Reprinted figure with permission from [86], Copyright 2017 by the American Physical Society.

Al-doped SiC, indicating that the spin polarization of C atoms contributes to the magnetic moments. It is in agreement with the XMCD study for ion-irradiated 6H-SiC [50].

### 3.6. Influence on nuclear spins

As a local probe technique, nuclear magnetic resonance (NMR) provides an impurity-insensitive way to get more insights into the magnetic properties of a material. In fact, the NMR spectrum measures the on-site internal hyperfine fields in a sample. For SiC, one can use  $^{13}\text{C}$  and  $^{29}\text{Si}$  NMR spectroscopy to study the defect-induced paramagnetism in neutron-irradiated 6H-SiC. The  $^{29}\text{Si}$  and  $^{13}\text{C}$  NMR spectra were acquired with a Hahn spin echo pulse sequence for temperatures of 2–100 K at a magnetic field of  $\mu_0 H = 7.100 \text{ T}$ . For the temperature-dependent measurements, the magnetic field was applied in the wafer plane.

Figure 26 shows the experimental  $^{13}\text{C}$  and  $^{29}\text{Si}$  NMR spectra for the neutron-irradiated 6H-SiC sample at temperatures between 2 and 100 K. As expected, only one spectral line of the transition  $I_z = -1/2 \rightarrow +1/2$  is observed for both isotopes due to their  $I = 1/2$  nuclear spin state. The full width at half maximum (FWHM) of the spectra at 100 K is below 5 kHz, which is very small for a solid sample, indicating the still high quality of the single crystal even after irradiation [52]. As the sample is cooled down, the FWHM becomes larger and is qualitatively attributed to the growing amplitude of the dipole magnetic field from the local moments of defects.

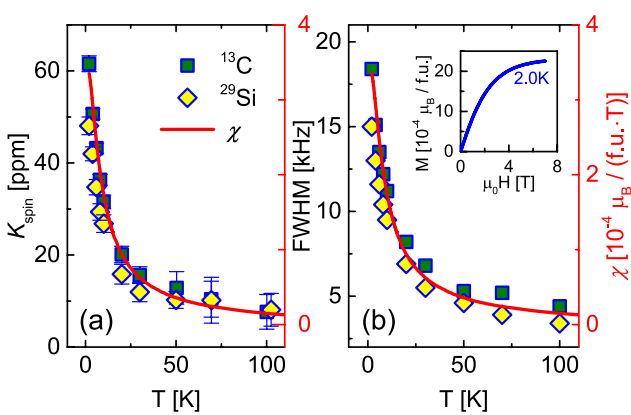


**Figure 27.** (a) Temperature dependence of spin part NMR shift  $K_{\text{spin}}$  for  $^{13}\text{C}$  and  $^{29}\text{Si}$  isotopes. (b) Temperature dependence of FWHM of  $^{13}\text{C}$  and  $^{29}\text{Si}$  NMR spectra. The identical red curves in (a) and (b) present the macroscopic susceptibility  $\chi(T)$  ( $\mu_0 H = 7$  T), and the inset of (b) shows the magnetization as a function of applied field at 2 K. Reprinted figure with permission from [86], Copyright 2017 by the American Physical Society.

The NMR shift  $K$  is defined as  $K = (f_{\text{res}} - f_0)/f_0$ , where  $f_0 = \gamma_n \mu_0 H / 2\pi$  is the Larmor frequency of a bare nucleus with a gyromagnetic ratio  $\gamma_n$  in a magnetic field  $\mu_0 H$ , and  $f_{\text{res}}$  is the NMR frequency.  $K$  is a combination of a spin part and an orbital part originating from the orbital moment:  $K = K_{\text{spin}} + K_{\text{orb}}$ .  $K_{\text{orb}}$  is generally temperature-independent. The spin part  $K_{\text{spin}} = A_{\text{hf}} \chi_{\text{spin}}$  is proportional to the static local susceptibility of the electronic spins at the nuclear site and to the hyperfine coupling  $A_{\text{hf}}$  between the nuclear spins and the electronic spins. The  $K_{\text{orb}}$  (or the  $K_{\text{spin}} = 0$  reference frequency) can be obtained from very sharp  $^{13}\text{C}$  and  $^{29}\text{Si}$  NMR spectra at 100 K of an unirradiated 6H-SiC sample.  $K_{\text{spin}}$  carries the information of defect-induced local moments.

The temperature dependence of the extracted  $K_{\text{spin}}$  and FWHM for both isotopes are shown in figures 27(a) and (b). The  $K_{\text{spin}}$  for both isotopes follows the Curie law, in agreement with the macroscopic magnetic susceptibility  $\chi(T)$  of the electron spins. The paramagnetism is also characterized by the Curie law behavior of the FWHM for both  $^{13}\text{C}$  and  $^{29}\text{Si}$  isotopes, which gives a quantitative description of the growing amplitude of the dipole field of local moments with decreasing temperature. These results are clear evidence for the intrinsic paramagnetism in the neutron-irradiated 6H-SiC.

In figure 28, we show the contour plot of the calculated  $K_{\text{spin}}$  in real space and the amplitude of  $K_{\text{spin}}$  is presented by colors. The local moments are indicated by the red-white-black singular points, where  $K_{\text{spin}}$  is divergently large but contributes little to the spectral weight due to its low volume fraction. The whole volume is split into positive and negative regions by the  $K_{\text{spin}} = 0$  black contour lines. A larger positive  $K_{\text{spin}}$  volume is shown and results in a positive peak position in the spectrum. Moreover, the majority of the nuclear sites have an average distance of a few nanometers from a nearby local moment. All NMR measurements and simulations provide a clear picture of the microscopic magnetic properties of the SiC sample at atomic scale.

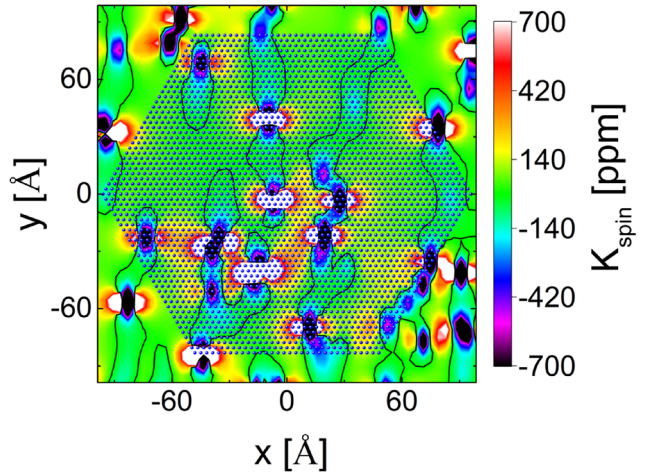


**Figure 28.** Simulation: contour plot of  $K_{\text{spin}}$  as a function of real space coordinates ( $x, y, z = 0$ ). Magnetic field is applied in plane, e.g. in the  $x$  (or  $a$ ) direction. The blue dots label the position of the nuclear sites, e.g. C atoms. The black solid lines label the positions where  $K_{\text{spin}} = 0$ . Reprinted figure with permission from [86], Copyright 2017 by the American Physical Society.

## 4. Applications

### 4.1. Spintronics

The word ‘spintronics’ (short for ‘spin electronics’) refers to devices in which we can manipulate the spin degree of freedom in a similar manner as manipulating charge. Spintronic devices can drastically improve computation speed and reduce power consumption. Defect-induced magnetism in semiconductors reveals a high Curie temperature and in principle provides an alternative for dilute ferromagnetic semiconductors in spintronic applications. The prerequisite is the interaction between the magnetism and free carriers in semiconductors.

For SiC, one can implant Al or N dopants to create carriers and defects simultaneously. In [78], the authors investigated magnetic and transport properties in ferromagnetic 4H-SiC single crystals prepared by post-implantation pulsed laser annealing. The implantation energies for Al and N were 180 keV and 110 keV, respectively. Samples were implanted with fluences from  $5 \times 10^{13}$  to  $5 \times 10^{16} \text{ cm}^{-2}$  for Al and from  $1 \times 10^{14}$  to  $1 \times 10^{17} \text{ cm}^{-2}$  for N, respectively. Pulsed laser annealing was performed in ambient air with a 308 nm excimer laser with pulse duration of about 30 ns. The energy density was 0.2, 0.4, 0.6, 0.8 J cm $^{-2}$ .

Figure 29(a) shows the magnetization versus magnetic field in the range of 5 kOe at 5 K. Before annealing, only diamagnetic features can be observed in the as-implanted samples due to the heavy lattice damage [53]. After annealing with a low energy  $0.2 \text{ J cm}^{-2}$ , a weak hysteresis loop can be observed in a small field range. With increasing pulsed laser energies, the magnetic order is gradually enhanced. A distinct hysteresis loop with ferromagnetic features can be clearly seen and the saturation magnetization reaches  $5 \times 10^{-4} \text{ emu g}^{-1}$  in the sample annealed using  $0.6 \text{ J cm}^{-2}$ . Then, the saturation in the  $0.8 \text{ J cm}^{-2}$  decreases compared with that in  $0.6 \text{ J cm}^{-2}$ . At 300 K, the diamagnetism increases slightly while the hysteresis loop is similar as shown in figure 29(b). So the room temperature ferromagnetism is induced by post-implantation

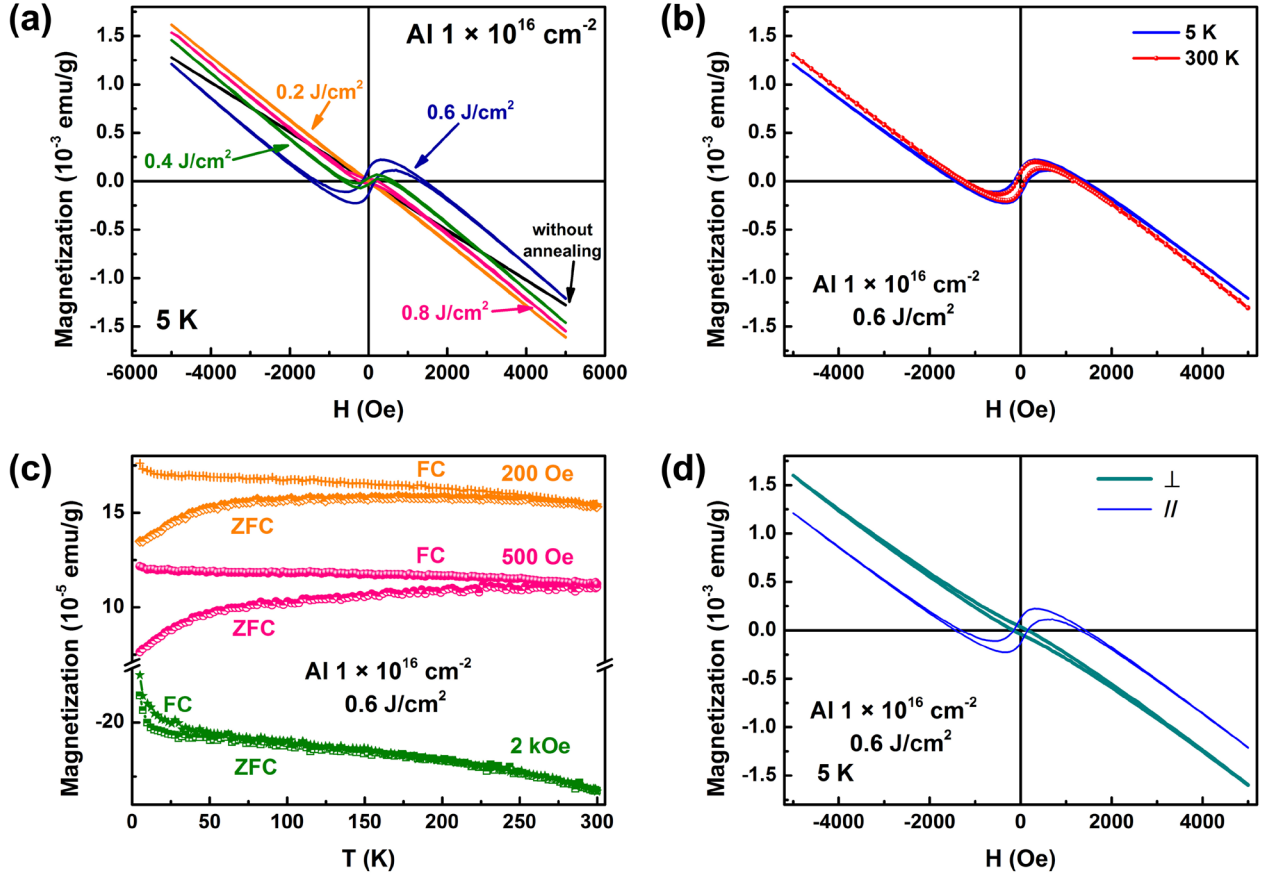


**Figure 29.** The magnetic properties of Al-implanted 4H-SiC after pulsed laser annealing. (a) The magnetization as a function of magnetic field within 5 kOe at 5 K. (b) The magnetization versus field for the sample annealed with the energy density of  $0.6 \text{ J cm}^{-2}$  at 5 K and 300 K. (c) ZFC/FC magnetization as a function of temperature from 5 K to 300 K under magnetic fields of 200, 500 and 2000 Oe. (a)–(c) The magnetic field was applied parallel to the sample surface. (d) The magnetization as a function of magnetic field measured with the field both perpendicular and parallel to the sample surface ( $000 -1$ ) within 5 kOe. Clear magnetic anisotropy is observed. Reprinted figure with permission from [78], Copyright 2017 by the American Physical Society.

annealing. The absence of tiny parasitic or any secondary magnetic phase is confirmed by the smooth and featureless magnetization versus temperature curve (figure 29(c)). Weak paramagnetism due to irradiation damage is also observed when the field of 2 kOe is applied. Figure 29(d) shows the magnetization measured with fields perpendicular and parallel to the sample surface ( $000 -1$ ), i.e. C face, at 5 K. The in-plane direction is found to be the easy axis. The  $ab$ -plane spin coupling is stronger than along the  $c$  axis, which could be the reason for this magnetic anisotropy [52]. Shape anisotropy is another contribution since the implanted layers are very thin. Nevertheless, the anisotropy corroborates that the magnetism is intrinsic, as foreign contamination or clusters are unlikely to bring either crystalline or shape anisotropy.

In the Hall effect measurement, the hole concentration and the mobility in SiC implanted with the Al fluence of  $1 \times 10^{16} \text{ cm}^{-2}$  after  $0.6 \text{ J cm}^{-2}$  pulsed laser annealing are estimated to be  $3.4 \times 10^{20} \text{ cm}^{-3}$  and  $0.40 \text{ cm}^2/(\text{Vs})$ , respectively, while they are  $2.3 \times 10^{20} \text{ cm}^{-3}$  and  $0.02 \text{ cm}^2/(\text{Vs})$  for the  $0.8 \text{ J cm}^{-2}$  sample. In the low field range, the trace of the anomalous Hall effect is observed in figure 30(a). The weak and noisy signal is probably due to the low carrier mobility. Weak negative magnetoresistance is observed in the samples annealed with

$0.6 \text{ J cm}^{-2}$  and  $0.8 \text{ J cm}^{-2}$  shown in figure 30(b). Negative magnetoresistance of the  $0.6 \text{ J cm}^{-2}$  sample can reach  $-1.5\%$  under 50 kOe at 2 K, while at 5 K it is almost the same as that of the  $0.8 \text{ J cm}^{-2}$  sample. The negative magnetoresistance decreases as the temperature increases and vanishes above 50 K. In contrast to Al-implanted SiC, ferromagnetism is much weaker in N-implanted SiC.

The anomalous Hall effect and negative magnetoresistance show that the internal magnetic field from spin ordering can influence the behavior of carriers. So the interaction exists between moments induced by divacancies and carriers due to doping. However, the anomalous Hall effect is very weak. It is probably due to the fact that the defect-induced magnetism is weak and the carrier mobility is low.

#### 4.2. Magnetometry as a measure of defects

As we have shown in previous sections, the amount of paramagnetic centers is proportional to the concentration of defects. Therefore, paramagnetism in ion- or neutron-irradiated SiC can be taken as a quantitative measurement for defects. It is particularly useful when the amount of defects is rather low or not enough for some techniques, such as RBS/C

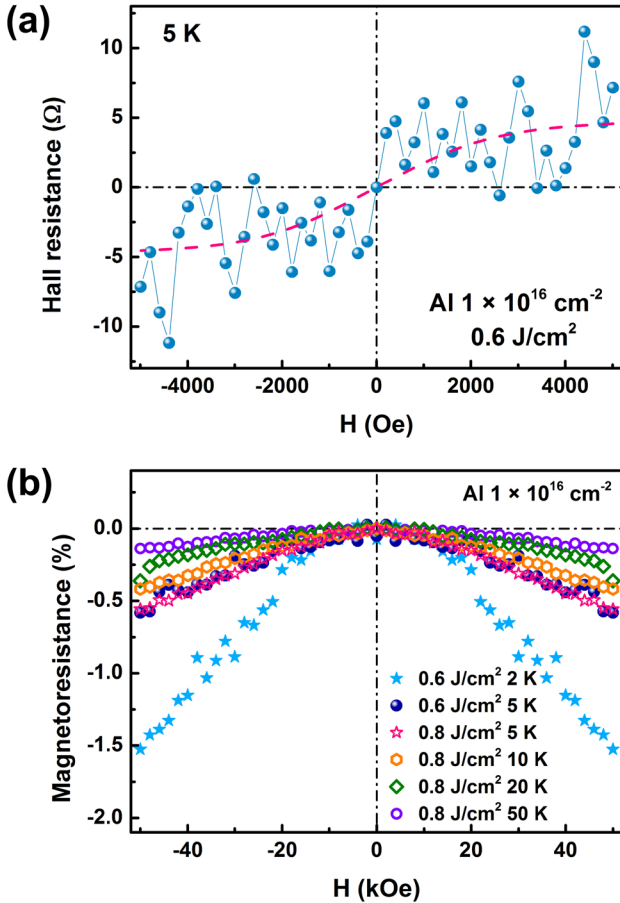


**Figure 30.** The magneto-transport properties of Al-implanted 4H-SiC after pulsed laser annealing. (a) The Hall resistance of the  $0.6 \text{ J cm}^{-2}$  sample with the field between  $\pm 5 \text{ kOe}$  at 5 K. The pink dashed line is a guide to the eye. (b) The magnetoresistance of the  $0.6 \text{ J cm}^{-2}$  and  $0.8 \text{ J cm}^{-2}$  samples in the field range of  $\pm 50 \text{ kOe}$ . Reprinted figure with permission from [78], Copyright 2017 by the American Physical Society.

[87–89] and transmission electron microscopy [1, 52, 89, 90], due to their detection limits.

As an example, figure 31 shows the concentration of paramagnetic centers (divacancies) depending on neutron fluence. The scaling between the concentration of paramagnetic centers and the neutron fluence provides a qualitative approach to measure irradiation-induced defects by a magnetometry method. The concentration of defects increases with irradiation fluence, in agreement with the characterization by Raman. It is beyond the sensitivity of transmission electron microscopy to measure those point defects [52].

Figure 32 shows the paramagnetic component for Al-implanted 4H-SiC. The paramagnetism also scales up with the Al fluence. The concentration of point defects, which is related to the density of paramagnetic centers, is determined by fitting the paramagnetic component of the specimen to the Brillouin function [91].

#### 4.3. Magnetic refrigeration

Magnetic refrigeration has been developed over many years by using the adiabatic demagnetization of electron spins in

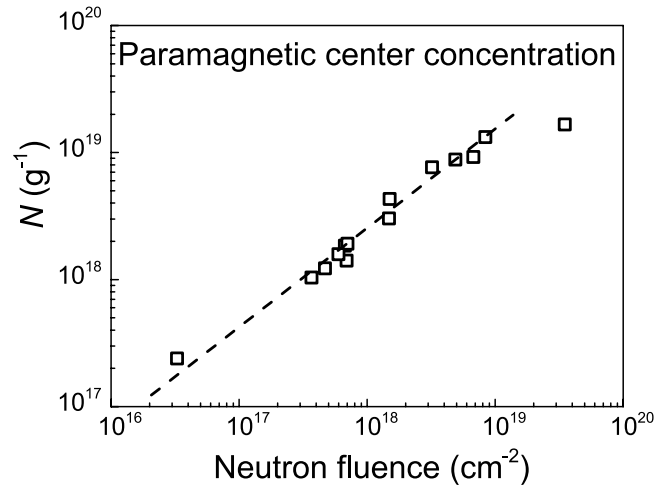


**Figure 31.** The fitted  $N$  (the density of paramagnetic centers) for 4H-SiC samples with different neutron fluence. The dashed line is only for guiding the eye to indicate the trend. Reprinted figure with permission from [52], Copyright 2015 by the American Physical Society.

paramagnetic salt powders at the milliKelvin temperature range and nuclear spins in metals at the sub-milliKelvin temperature range [92]. As we show that paramagnetism can be induced in SiC by irradiation, Vlasov *et al* proposed paramagnetic semiconductors, including SiC, as active media for refrigeration at cryogenic temperatures by adiabatic demagnetization [93]. Paramagnetism can come from un-ionized impurity dopants or structural defects, both contributing to local magnetic moments.

The specific spin entropy  $\delta\zeta = k_B N_s \ln(2J + 1)$  available for magnetic refrigeration for SiC and other material systems can be calculated by using the experimentally measured spin density  $N_s$  and angular momentum  $J$ . The results are shown in figure 33. It is shown that for doped semiconductors a large spin density is achievable in larger gap semiconductors (such as SiC). Neutron irradiation provides another method of introducing paramagnetism to semiconductors. A spin-1 density of  $N_s$  around  $5.3 \times 10^{19} \text{ cm}^{-3}$  can be obtained in neutron-irradiated 4H-SiC [52]. The simulated temperatures are shown in figure 34 for neutron-irradiated 4H-SiC, Si:P and GaN:Mn with particular spin and electron concentrations. The initial temperature was set equal to that of a reservoir at  $T_0 = 300 \text{ mK}$ , and the zero-field time constant  $\tau_0 = 3600 \text{ s}$  represents a weak thermal link. The magnetic field profile was swept from an initial field  $B_i$  to a final field  $B_f$  at a constant sweep rate of 100 mT/min. As shown by this simulation, it is possible to achieve a base temperature below 50 mK.

The authors also pointed out that semiconductors, including SiC, are the most common substrate used for electronic and micro-electromechanical devices and thus offer the possibility of monolithic integration of solid state refrigerants with active devices [93].

#### 4.4. Defects for quantum technology

The successful implementation of the nitrogen-vacancy (NV) center in diamond as a qubit has attracted a great deal of

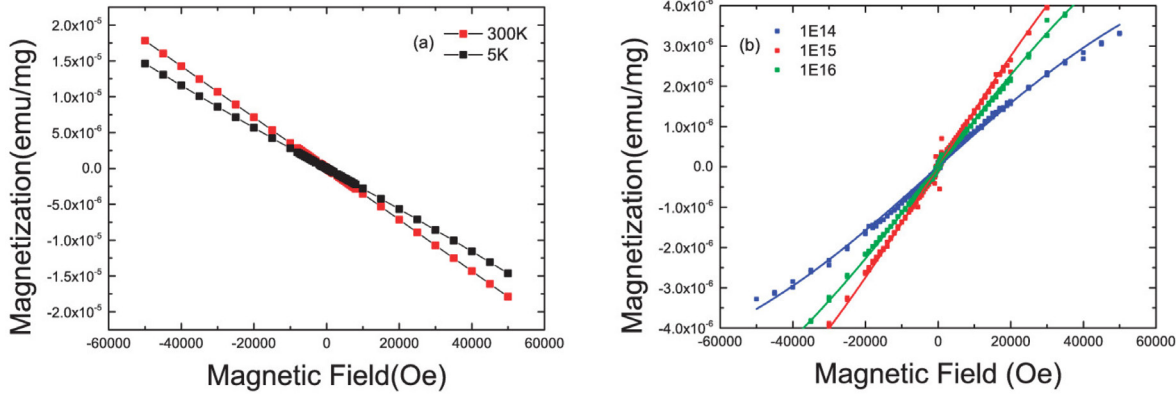


**Figure 32.** (a) Magnetization versus field curves of the pristine 4H-SiC sample at 5 K and 300 K. (b) Paramagnetic component of samples 1E14, 1E15 and 1E16 (the numbers are implantation fluence in  $\text{cm}^{-2}$ ) at 5 K and the Brillouin fitting curve. Reproduced from [91]. CC BY 4.0.

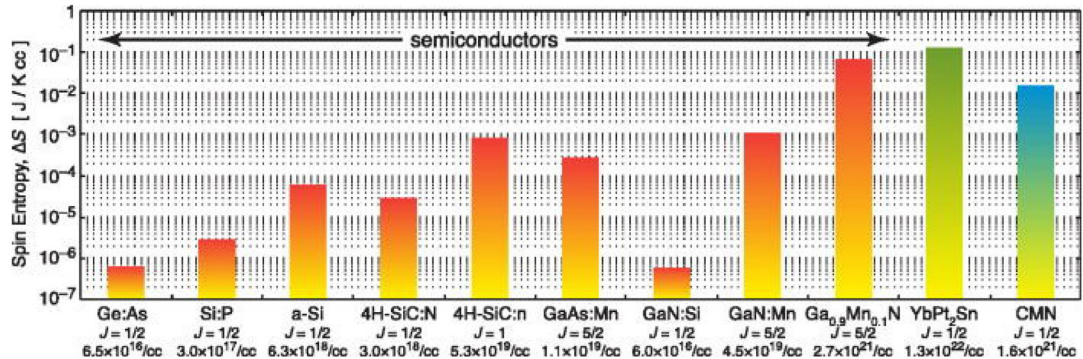


**Figure 33.** The theoretical spin entropy of different semiconductor systems. The values of the intermetallic compound YbPt<sub>2</sub>Sn and the commonly used paramagnetic salt CMN are shown as reference. The experimentally measured spin- $J$  and spin density  $N_s$  are indicated for each system. Reprinted from [93], with the permission of AIP Publishing.

interest to utilize defects for quantum technology. In principle, similar defects can exist in other material systems. Indeed, in SiC the silicon vacancy was found to combine the technological advantages of semiconductor quantum dots and the unique spin properties of the NV center in diamond [94]. A carbon antisite-vacancy pair in 4H-SiC created by electron irradiation and annealing was proposed to build room temperature, photo-stable single-photon sources [95]. von Bardeleben *et al* showed that NV triplet centers can also be generated in all the main SiC polytypes as a platform for solid-state qubits and nanosensors [96]. Much different from diamond, SiC is already technologically and industrially relevant, due to its applications in high-frequency and high-power devices. Therefore, SiC offers a device-friendly platform for quantum technology. For details, we recommend a recent review paper by Ohshima *et al* [97].

## 5. Challenges

### 5.1. Contamination of transition metal impurities

Although defect-induced magnetism has been reported in many material systems, the measured magnetization remains as a weak signal slightly above the detection limit of sensitive SQUID magnetometry. On one hand, measurement artifacts in SQUID magnetometry may occur: the improper mounting of samples and wrong use of sample holders can easily generate

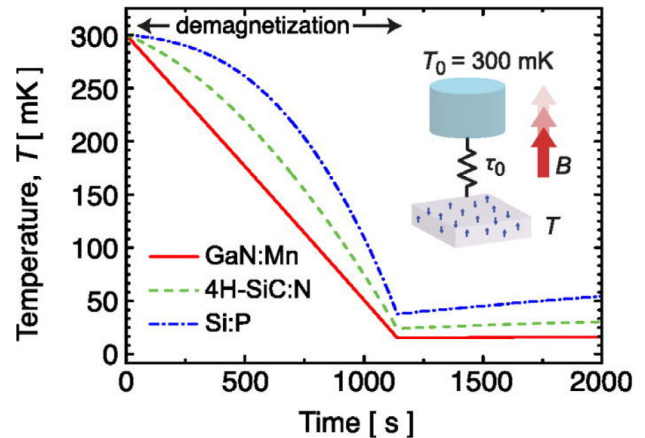


**Figure 34.** The simulated temperature  $T$  versus time  $t$  of Si:P, 4H-SiC:N and GaN:Mn with particular spin and electron concentrations, connected to a reservoir at  $T_0 = 300$  mK through a zero-field time constant of  $\tau_0 = 3600$  s. The initial magnetic field of  $B_i = 2.0$  T is swept to a final field of  $B_f = 0.1$  T at a sweep rate of  $100$  mT min<sup>-1</sup>. Reprinted from [93], with the permission of AIP Publishing.

ferromagnetic-like signals [98, 99]. On the other hand, there is always a debate over the purity of graphite and oxide substrates [100, 101]. Indeed, SiC has been developed to the microelectronic grade and contains fewer impurities.

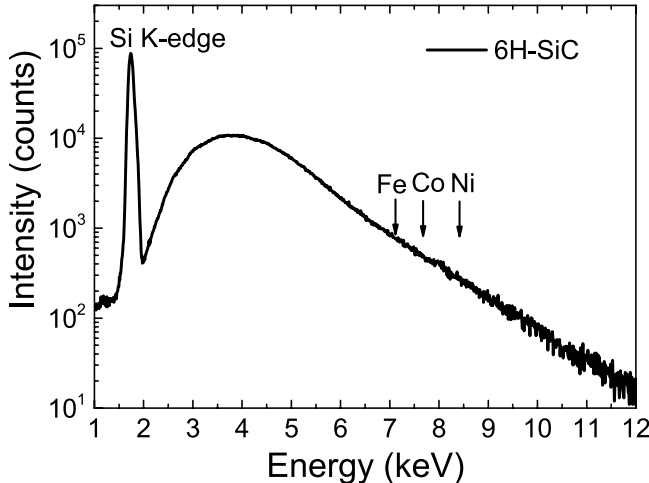


**Figure 35.** PIXE spectrum for high-purity, semi-insulating 6H-SiC wafer using a broad proton beam. Within the detection limit, no Fe, Co or Ni contamination is observed. Reproduced from [50]. CC BY 4.0.

To check the trace presence of transition metals (Fe, Co, Ni, etc) in high-purity semi-insulating (HPSI) SiC substrates, PIXE presents a useful method with its bulk sensitivity of ppm amplitude without significant structural destruction [101]. One measurement for 6H-SiC is shown in figure 35 using 2 MeV protons with a broad beam of around  $1\text{ mm}^2$ . In the spectrum, the sharp peak is the Si K-line x-ray emission. The broad bump is due to the secondary electron Bremsstrahlung background. For commercially available purest graphite, there is detectable transition metal contamination (mainly Ti, V, Fe and Ni) as revealed by PIXE [101]. However, the transition metal impurity in the HPSI SiC, if any, is below the detection limit of around 1 ppm (figure 35). Nevertheless, the sample purity should be carefully checked for studying defect-induced magnetism.

On the other hand, the possible influence of low-concentration impurities on the magnetism has been discussed in published papers. Shi *et al* grew undoped and V-doped 6H-SiC single crystals by the physical vapor transport method [102]. The V concentration was determined to be  $3.76 \times 10^{17}$  at.  $\text{cm}^{-3}$  and  $6.14 \times 10^{17}$  at.  $\text{cm}^{-3}$  by secondary ion mass spectrometry for low V-doped and high V-doped SiC samples, respectively. The undoped 6H-SiC shows only diamagnetism, but the V-doped 6H-SiC reveals ferromagnetism. The sample with lower V concentration shows stronger ferromagnetism compared to that with higher V concentration. It is suggested that both V dopants and defects are essential for introducing ferromagnetism in V-doped SiC. In [103], the authors prepared Mn-doped 6H-SiC with Mn concentration below  $10^{-3}$  molar fraction. The typical ferromagnetic order was established at a Mn-doped concentration as low as  $10^{-4}$  molar fraction at around 250 K. The authors speculated that the defect-related effects other than the Mn content play a more important role in determining the magnetic ordering. However, the Mn impurities probably stabilize the wanted defects.

### 5.2. Spatial correlation between defects and magnetism

In many published results regarding defect-induced magnetism, there are hints that the ferromagnetism is not homogeneous. In [52, 67], the authors speculated that the ferromagnetic coupling can occur locally in some regions with proper defect concentration. For 3C-SiC, Liu *et al* disclosed that local magnetism is only on the (110) and (001) surfaces [104]. Esmaeily *et al* measured the magnetic properties of nanoporous alumina ( $\text{Al}_2\text{O}_3$ ) membranes [105]. These membranes exhibit a temperature-independent and almost anhysteretic saturating response to a magnetic field up to temperatures of 300 K or higher. The magnetism increases with the area of the open nanopores. Crystallization of the membrane or treatment with salicylic acid can destroy 90% of the magnetism. The authors suggested that the effect is linked with the surfaces of the open pores in amorphous  $\text{Al}_2\text{O}_3$ .

Therefore, one needs an experiment which can measure the spatial distribution of ferromagnetism. Muon spin relaxation ( $\mu\text{SR}$ ) measurements provide such a possibility. In  $\mu\text{SR}$  experiments, spin-polarized positive muons are implanted into materials. Each muon stopped in the lattice experiences the external and local magnetic fields and therefore precesses at a characteristic frequency. In experiments, the time evolution of the muon polarization  $P(t)$  is measured to get information about the interaction of the muon magnetic moment with its magnetic environment. A single precession frequency is expected in a spatially homogenous ferromagnet or antiferromagnet. If the muons experience inhomogeneous magnetic fields,  $P(t)$  shows a distribution of precession frequencies (a ‘line shape’) with the corresponding width. In a paramagnetic environment  $P(t)$  exhibits only slow exponential relaxation. Therefore, the local magnetic field distributions can be obtained on the atomic scale by  $\mu\text{SR}$ . The sensitivity allows the measurement of the internal magnetic fields below 0.1 Gauss in materials with very dilute magnetic moments [106, 107], ideally suitable for investigating defect-induced magnetism.

$\mu\text{SR}$  measurements were applied to investigate defect-induced magnetism in ZnO [106, 107]. The magnetic volume was measured by the relaxing amplitude. For ZnO nanoparticles [106], the strongest relaxation was found for the fine-grained sample, corresponding to a total magnetic volume fraction of about 35%. For the large-grained sample, the magnetic volume fraction was approximately 15%. For ferromagnetic ZnO films, the volume fraction of the ferromagnetism phase was approximately 70%. Both studies suggest that the defect-induced ferromagnetism in ZnO is not homogeneous. Similar experiments are expected for SiC.

### 5.3. Controlling charge states of defects

As we have discussed, the electronic structure of defects will depend on their charge states. However, it is challenging to manipulate the charge state in a controllable manner. In [77], the authors have suggested that nitrogen doping to substitute

C atoms can manipulate the charge states of Si vacancy defects in 3C-SiC and the magnetic interactions between them [77]. We attempted to work on this issue by N and Al doping in 4H-SiC. The results show the opposite behavior [78]. In Al-implanted SiC, relatively strong ferromagnetism was observed, but in N-implanted SiC, the ferromagnetism was much weaker. The reason is still unclear.

The charge states of both divacancies and Si vacancies have been demonstrated to be controllable by optical excitation with different wavelengths [108–110]. For instance, under excitation at energy levels below 1.3 eV,  $V_{Si^-}V_C$  divacancies are switched from neutral to positively charged states [108]. This also gives perspective to control the defect-induced magnetism in SiC by light.

## 6. Summary and outlook

Defect-induced ferromagnetism in ion-implanted and neutron-irradiated SiC has been observed by us and other groups. Some typical features describing conventional ferromagnetic materials are also observed in SiC, such as the magnetization dependence on the defect concentration, magnetic anisotropy, anomalous Hall effect (although very weak) and x-ray magnetic circular dichroism. These features in combination with first-principles calculations demonstrate the intrinsic nature of the observed magnetism. However, there are still many questions unanswered. We list some of them as suggestions for future investigations.

### (1) Local identification of the ferromagnetic regions or domains in SiC

From the investigations of ion-implanted and neutron-irradiated SiC, there is an accumulation of evidence that ferromagnetic coupling does not occur homogeneously in the sample. The ferromagnetism is distributed non-homogeneously in terms of its lateral distribution or depth distribution. Moreover, we are still uncertain if ferromagnetic domains with allowed orientations exist just like normal ferromagnets.  $\mu$ SR measurements might be applied to confirm this speculation. A careful magnetic field microscopy investigation to scan over the surface is also a good means to this end. For the depth distribution, physical or chemical etching could be used to control the affected depth. Moreover, together with step-by-step magnetization measurement, one can probably identify the depth profile of the magnetization. Such an investigation may allow us to identify whether the ferromagnetism is mainly at the surface, near some extended defects or dependent on the irradiation depth.

Another possible method is nuclear probe  $^{57}\text{Fe}$ . By implanting  $^{57}\text{Fe}$  probe atoms, point defects and disorder will be created around these implanted probes and conversion electron Mössbauer spectroscopy can be performed. By measuring electric quadrupole and magnetic

interactions simultaneously, magnetic properties will be obtained in the probe atomically local environment [111], providing us insight into the defect-induced magnetism in SiC at the atomic level.

### (2) Magnetic state of a single defect in SiC

By scanning tunneling microscopy experiments, Ugeda *et al* observed a sharp electronic resonance at the Fermi energy around a single vacancy in graphite, which may be associated with the formation of a local magnetic moment [63]. In the future, such an experiment for SiC should be feasible to clarify the magnetic state of a single defect. Scanning tunneling microscopy has been used to reveal the atomic structure at the surface of 6H-SiC [112].

### (3) Thermal stability of defect-induced ferromagnetism in SiC

The thermal stability is the key factor for potential application because some defects will recombine or even disappear at room temperature. Sometimes the neutralization occurring at room temperature will also lead to loss of the ferromagnetism. This is the major reason for the volatility of memory devices. Moreover, it will lead to a better understanding of the thermal dynamics of the defects, especially in the paramagnetic regime. The annealing methods include a high-temperature oven, rapid thermal annealing and sub-second annealing by flashlamps [113] and a high-power pulse excimer laser. The aim is to confirm whether the slightly damaged SiC can be completely recrystallized, i.e. recovered to the quality of the virgin SiC, and to investigate the evolution of magnetic and optical properties at different annealing stages.

### (4) Optical and electrical control of magnetism in SiC

One of the advantages of semiconductor materials exhibiting magnetism is the control of magnetism by optical and electrical methods without altering the semiconducting properties. Such control has been demonstrated for GaMnAs by optical excitation and by electrical gating at low temperatures [114]. SiC with defect-induced magnetism may provide such a test platform at room temperature.

## Acknowledgments

The work was financially supported by the Helmholtz-Gemeinschaft Deutscher Forschungszentren (VH-NG-713) and by the Beijing Municipal Science and Technology Project (Grant Nos. Z171100002217004, D171100004517001 and Z161100002116018). S Z thanks the ion implantation group at the Ion Beam Center, HZDR. The authors are grateful to Manfred Helm for his critical reading of the manuscript.

## ORCID iDs

Shengqiang Zhou  <https://orcid.org/0000-0002-4885-799X>

## References

- [1] Stromberg F, Keune W, Chen X, Bedanta S, Reuther H and Mücklich A 2006 *J. Phys.: Condens. Matter* **18** 9881
- [2] Diallo M *et al* 2015 *J. Appl. Phys.* **117** 183907
- [3] Dietl T 2002 *Semicond. Sci. Technol.* **17** 377
- [4] Esquinazi P, Spemann D, Höhne R, Setzer A, Han K H and Butz T 2003 *Phys. Rev. Lett.* **91** 227201
- [5] Xia H *et al* 2008 *Adv. Mater.* **20** 4679–83
- [6] Yang X, Xia H, Qin X, Li W, Dai Y, Liu X, Zhao M, Xia Y, Yan S and Wang B 2009 *Carbon* **47** 1399–406
- [7] Coey J M D, Stamenov P, Gunning R, Venkatesan M and Paul K 2010 *New J. Phys.* **12** 053025
- [8] Song B, Bao H, Li H, Lei M, Peng T, Jian J, Liu J, Wang W, Wang W and Chen X 2009 *J. Am. Chem. Soc.* **131** 1376–7
- [9] Yi J *et al* 2010 *Phys. Rev. Lett.* **104** 137201
- [10] Sundaresan A, Bhargavi R, Rangarajan N, Siddesh U and Rao C N R 2006 *Phys. Rev. B* **74** 161306
- [11] Garcia M *et al* 2007 *Nano Lett.* **7** 1489–94
- [12] Volnianska O and Boguslawski P 2010 *J. Phys.: Condens. Matter* **22** 073202
- [13] Esquinazi P, Hergert W, Spemann D, Setzer A and Ernst A 2013 *IEEE Trans. Magn.* **49** 4668–74
- [14] Zhou S 2014 *Nucl. Instrum. Methods Phys. Res. B* **326** 55–60
- [15] Kimoto T 2015 *Japan. J. Appl. Phys.* **54** 040103
- [16] Ramsdell L S 1947 *Am. Mineral.* **32** 64–82
- [17] Casady J and Johnson R W 1996 *Solid State Electron.* **39** 1409–22
- [18] Powell A R and Rowland L B 2002 *Proc. IEEE* **90** 942–55
- [19] Torpo L, Marlo M, Staab T and Nieminen R 2001 *J. Phys.: Condens. Matter* **13** 6203
- [20] Weber J, Koehl W, Varley J, Janotti A, Buckley B, Van de Walle C and Awschalom D 2011 *J. Appl. Phys.* **109** 102417
- [21] Bechstedt F, Fissel A, Furthmüller J, Grossner U and Zywietz A 2001 *J. Phys.: Condens. Matter* **13** 9027
- [22] Kimoto T, Nakazawa S, Hashimoto K and Matsunami H 2001 *Appl. Phys. Lett.* **79** 2761–3
- [23] Fujihira K, Kimoto T and Matsunami H 2002 *Appl. Phys. Lett.* **80** 1586–8
- [24] Zhang J, Storasta L, Bergman J, Son N and Janzen E 2003 *J. Appl. Phys.* **93** 4708–14
- [25] Ziegler J F, Ziegler M and Biersack J 2010 *Nucl. Instrum. Methods Phys. Res. B* **268** 1818–23
- [26] Devanathan R and Weber W J 2000 *J. Nucl. Mater.* **278** 258–65
- [27] Krasheninnikov A and Nordlund K 2010 *J. Appl. Phys.* **107** 3
- [28] Storasta L, Bergman J, Janzen E, Henry A and Lu J 2004 *J. Appl. Phys.* **96** 4909–15
- [29] Chen X D, Yang C L, Gong M, Ge W K, Fung S, Beling C D, Wang J N, Lui M K and Ling C C 2004 *Phys. Rev. Lett.* **92** 125504
- [30] Wendler E *et al* 2012 *Nucl. Instrum. Methods Phys. Res. B* **286** 97–101
- [31] Kelly B, Marsden B, Hall K, Martin D, Harper A and Blanchard A 2000 *IAEA Tecdoc* **1154**
- [32] Cartz L, Karioris F, Roult G and Labbe J 1984 *Radiat. Eff.* **85** 57–9
- [33] Zvanut M E 2004 *J. Phys.: Condens. Matter* **16** R1341
- [34] Isoya J, Umeda T, Mizuochi N, Son N, Janzen E and Ohshima T 2008 *Phys. Status Solidi B* **245** 1298–314
- [35] Son N, Hai P, Wagner M, Chen W, Ellison A, Hallin C, Monemar B and Janzen E 1999 *Semicond. Sci. Technol.* **14** 1141
- [36] Gordon L, Janotti A and Van de Walle C G 2015 *Phys. Rev. B* **92** 045208
- [37] Koehl W F, Buckley B B, Heremans F J, Calusine G and Awschalom D D 2011 *Nature* **479** 84
- [38] Pensl G and Choyke W J 1993 *Physica B* **185** 264–83
- [39] Hemmingsson C, Son N T, Kordina O, Bergman J, Janzen E, Lindström J, Savage S and Nordell N 1997 *J. Appl. Phys.* **81** 6155–9
- [40] David M, Alfieri G, Monakhov E, Hallén A, Blanchard C, Svensson B and Barbot J 2004 *J. Appl. Phys.* **95** 4728–33
- [41] Ayedh H, Nipoti R, Hallén A and Svensson B 2015 *Appl. Phys. Lett.* **107** 252102
- [42] Ahmed E M H 2008 Characterization of control mesoporous glasses (CPGs) using positron annihilation lifetime spectroscopy (PALS) *PhD Thesis* Martin Luther University Halle-Wittenberg
- [43] Rempel A and Schaefer H E 1995 *Appl. Phys. A* **61** 51–3
- [44] Ling C, Deng A, Fung S and Beling C 2000 *Appl. Phys. A* **70** 33–8
- [45] Ling C, Beling C and Fung S 2000 *Phys. Rev. B* **62** 8016
- [46] Brauer G, Anwand W, Coleman P, Störmer J, Plazaola F, Campillo J, Pacaud Y and Skorupa W 1998 *J. Phys.: Condens. Matter* **10** 1147
- [47] Brauer G, Anwand W, Coleman P, Knights A, Plazaola F, Pacaud Y, Skorupa W, Störmer J and Willutzki P 1996 *Phys. Rev. B* **54** 3084
- [48] Liu Y, Wang G, Wang S, Yang J, Chen L, Qin X, Song B, Wang B and Chen X 2011 *Phys. Rev. Lett.* **106** 087205
- [49] Anwand W, Brauer G and Skorupa W 2002 *Appl. Surf. Sci.* **194** 131–5
- [50] Wang Y *et al* 2015 *Sci. Rep.* **5** 8999
- [51] Yu L, Jin H, Liu D, Dai Y, Guo M, Huang B and Zhang Z 2010 *Chem. Phys. Lett.* **496** 276–9
- [52] Wang Y *et al* 2015 *Phys. Rev. B* **92** 174409
- [53] Li L, Prucnal S, Yao S D, Potzger K, Anwand W, Wagner A and Zhou S 2011 *Appl. Phys. Lett.* **98** 222508
- [54] Weber W, Wang L, Yu N and Hess N 1998 *Mater. Sci. Eng. A* **253** 62–70
- [55] Wang Y *et al* 2014 *J. Appl. Phys.* **115** 17C104
- [56] Li L, Hua W, Prucnal S, Yao S D, Shao L, Potzger K and Zhou S 2012 *Nucl. Instrum. Methods Phys. Res. B* **275** 33–6
- [57] Zheng H, Yan Y, Lv Z, Yang S, Li X, Liu J, Ye B, Peng C, Diao C and Zhang W 2013 *Appl. Phys. Lett.* **102** 142409
- [58] He X, Tan J, Zhang B, Zhao M, Xia H, Liu X, He Z, Yang X and Zhou X 2013 *Appl. Phys. Lett.* **103** 262409
- [59] Lv Z, Ma X, Zheng H, An R, Peng C, Liu J, Ye B, Diao C, Liu X and Zhang W 2013 *Mater. Lett.* **93** 374–6
- [60] Zhou R W, Liu X C, Wang H J, Chen W B, Li F, Zhuo S Y and Shi E W 2015 *AIP Adv.* **5** 047146
- [61] Li Q, Xu J, Liu J and Ye B 2016 *Mater. Res. Exp.* **3** 056103
- [62] Lehtinen P O, Foster A S, Ma Y, Krasheninnikov A V and Nieminen R M 2004 *Phys. Rev. Lett.* **93** 187202
- [63] Ugeda M M, Brihuega I, Guinea F and Gómez-Rodríguez J M 2010 *Phys. Rev. Lett.* **104** 096804
- [64] Yazev O V 2010 *Rep. Prog. Phys.* **73** 056501
- [65] Wang Y, Pochet P, Jenkins C A, Arenholz E, Bukalis G, Gemming S, Helm M and Zhou S 2014 *Phys. Rev. B* **90** 214435
- [66] Semenov A, Pashchenko V, Khirnyi V, Kozlovskiy A and Mateichenko P 2015 *Physica E* **74** 220–5
- [67] Wang Y *et al* 2014 *Phys. Rev. B* **89** 014417
- [68] Bean C P and Livingston J D 1959 *J. Appl. Phys.* **30** S120
- [69] Shiratsuchi Y, Endo Y and Yamamoto M 2004 *Thin Solid Films* **464–5** 141–5
- [70] Zhou S *et al* 2009 *Phys. Rev. B* **80** 094409
- [71] Slawska-Waniewska A, Gutowski M, Lachowicz H K, Kulik T and Matyja H 1992 *Phys. Rev. B* **46** 14594
- [72] Jamet M *et al* 2006 *Nature Mater.* **5** 653–9
- [73] Thies A, Dederichs P H, Zeller R, Blügel S and Lambrecht W R L 2012 *Phys. Rev. B* **86** 180401
- [74] Qin S, Guo X, Cao Y, Ni Z and Xu Q 2014 *Carbon* **78** 559–65

- [75] Barzola-Quiquia J, Esquinazi P, Rothermel M, Spemann D, Butz T and García N 2007 *Phys. Rev. B* **76** 161403
- [76] Ramos M A, Barzola-Quiquia J, Esquinazi P, Muñoz Martin A, Climent-Font A and Garcia-Hernandez M 2010 *Phys. Rev. B* **81** 214404
- [77] Zhao M, Pan F and Mei L 2010 *Appl. Phys. Lett.* **96** 012508
- [78] Liu Y *et al* 2017 *Phys. Rev. B* **95** 195309
- [79] Morbec J M and Rahman G 2013 *Phys. Rev. B* **87** 115428
- [80] Stohr J, Padmore H, Anders S, Stammle T and Scheinfein M 1998 *Surf. Rev. Lett.* **5** 1297–308
- [81] Ney A *et al* 2010 *New J. Phys.* **12** 013020
- [82] Ohldag H, Esquinazi P, Arenholz E, Spemann D, Rothermel M, Setzer A and Butz T 2010 *New J. Phys.* **12** 123012
- [83] Gao X, Chen S, Liu T, Chen W, Wee A, Nomoto T, Yagi S, Soda K and Yuhara J 2008 *Phys. Rev. B* **78** 201404
- [84] Dedkov Y S and Fonin M 2010 *New J. Phys.* **12** 125004
- [85] He M, He X, Lin L, Song B and Zhang Z 2014 *Solid State Commun.* **197** 44–8
- [86] Zhang Z T, Dmytrieva D, Molatta S, Wosnitza J, Wang Y, Helm M, Zhou S and Kühne H 2017 *Phys. Rev. B* **95** 085203
- [87] Jiang W, Zhang Y and Weber W J 2004 *Phys. Rev. B* **70** 165208
- [88] Debelle A, Thomé L, Dompoint D, Boulle A, Garrido F, Jagielski J and Chaussende D 2010 *J. Phys. D: Appl. Phys.* **43** 455408
- [89] Malherbe J B 2013 *J. Phys. D: Appl. Phys.* **46** 473001
- [90] Heera V, Prokert F, Schell N, Seifarth H, Fukarek W, Voelksow M and Skorupa W 1997 *Appl. Phys. Lett.* **70** 3531–3
- [91] Peng B, Jia R X, Wang Y T, Dong L P, Hu J C and Zhang Y M 2016 *AIP Adv.* **6** 095201
- [92] Pobell F 1996 *Matter and Methods at Low Temperatures* vol 2 (Berlin: Springer)
- [93] Vlasov A, Guillemette J, Gervais G and Szkopek T 2017 *Appl. Phys. Lett.* **111** 142102
- [94] Riedel D, Fuchs F, Kraus H, Väth S, Sperlich A, Dyakonov V, Soltamova A, Baranov P, Ilyin V and Astakhov G 2012 *Phys. Rev. Lett.* **109** 226402
- [95] Castelletto S, Johnson B, Ivády V, Stavrias N, Umeda T, Gali A and Ohshima T 2014 *Nat. Mater.* **13** 151
- [96] Von Bardeleben H, Cantin J, Csóré A, Gali A, Raals E and Gerstmann U 2016 *Phys. Rev. B* **94** 121202
- [97] Ohshima T, Satoh T, Kraus H, Astakhov G V, Dyakonov V and Baranov P G 2018 *J. Phys. D: Appl. Phys.* **51** 333002
- [98] Sawicki M, Stefanowicz W and Ney A 2011 *Semicond. Sci. Technol.* **26** 064006
- [99] Pereira L, Araújo J, Van Bael M, Temst K and Vantomme A 2011 *J. Phys. D: Appl. Phys.* **44** 215001
- [100] Sepioni M, Nair R R, Tsai I L, Geim A K and Grigorieva I V 2012 *Europhys. Lett.* **97** 47001
- [101] Spemann D, Esquinazi P, Setzer A and Böhlmann W 2014 *AIP Adv.* **4** 107142
- [102] Shi-Yi Z, Xue-Chao L, Ze X, Wen-Sheng Y, Jun X, Jian-Hua Y and Er-Wei S 2012 *Chin. Phys. B* **21** 067503
- [103] Song B, Bao H, Li H, Lei M, Jian J, Han J, Zhang X, Meng S, Wang W and Chen X 2009 *Appl. Phys. Lett.* **94** 102508
- [104] Liu L Z, Wu X L, Liu X X, Xiong S J and Chu P K 2014 *J. Phys. Chem. C* **118** 25429–33
- [105] Esmaeil A S, Venkatesan M, Sen S and Coey J 2018 *Phys. Rev. Mater.* **2** 054405
- [106] Tietze T *et al* 2015 *Sci. Rep.* **5** 8871
- [107] Tseng L *et al* 2017 *Phys. Rev. B* **96** 104423
- [108] Golter D and Lai C 2017 *Sci. Rep.* **7** 13406
- [109] Wolfowicz G, Anderson C P, Yeats A L, Whiteley S J, Niklas J, Poluektov O G, Heremans F J and Awschalom D D 2017 *Nat. Commun.* **8** 1876
- [110] Magnusson B, Son N T, Csóré A, Gällström A, Ohshima T, Gali A and Ivanov I G 2018 *Phys. Rev. B* **98** 195202
- [111] Sielemann R, Kobayashi Y, Yoshida Y, Gunnlaugsson H P and Weyer G 2008 *Phys. Rev. Lett.* **101** 137206
- [112] Li L and Tsong I 1996 *Surf. Sci.* **351** 141–8
- [113] Rebohle L, Prucnal S and Skorupa W 2016 *Semicond. Sci. Technol.* **31** 103001
- [114] Nazmul A M, Kobayashi S, Sugahara S and Tanaka M 2004 *J. Appl. Phys.* **43** L233